ACS Photonics

Article

pubs.acs.org/journal/apchd5

Energy Losses and Transition Radiation in Multilayer Graphene Traversed by a Fast Charged Particle

Kamran Akbari,[*,†] Zoran L. Mišković,[*,†,‡] Silvina Segui,[*,§,∥] Juana L. Gervasoni,[§,∥,⊥] and Néstor R. Arista[§,⊥]

[†]Department of Applied Mathematics and [‡]Waterloo Institute for Nanotechnology, University of Waterloo, Waterloo, Ontario Canada N2L 3G1

[§]Centro Atómico Bariloche, Comisión Nacional de Energía Atómica, Av. Bustillo 9500, 8400 S.C. de Bariloche, Argentina

[∥]Consejo Nacional de Investigaciones Científicas y Técnicas of Argentina (CONICET), Argentina

[⊥]Instituto Balseiro, Universidad Nacional de Cuyo, S.C. de Bariloche, Argentina

Supporting Information

ABSTRACT: We present a fully relativistic formulation of the energy loss of a charged particle traversing a number of graphene layers and apply it to the case of two spatially separated layers probed by an energetic electron. We focus on the THz frequency range, using a Drude model to describe the conductivity of graphene and allowing for different doping density in each layer. We distinguish two types of contributions to the electron energy loss: the energy deposited in graphene layers in the form of electronic excitations (Ohm losses), which include the excitation of Dirac plasmon polaritons (DPP), and the energy that is emitted in the form of transition radiation. We study in detail the contribution of each layer to the ohmic losses and analyze the directional decomposition of the radiation emitted in the half-spaces defined by the graphene planes. By increasing the interlayer distance and changing the relative doping densities in graphene layers, we find surprisingly strong asymmetries in both the directional and layer-wise decompositions with respect to the direction of motion of the external electron. A modal decomposition is also performed in the limit of vanishing damping in graphene, exposing quite intricate roles of bonding and antibonding hybridization between DPPs in ohmic losses.

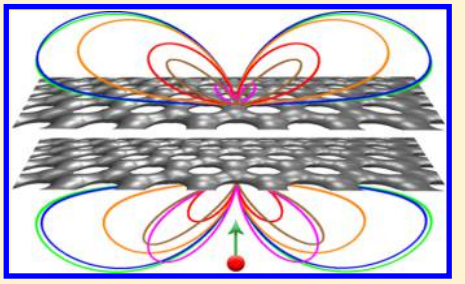

KEYWORDS: *graphene, electron energy loss, retardation effects, Dirac plasmon, transition radiation*

The study of plasmons in graphene is the subject of a vast experimental and theoretical effort in the last years, due to its remarkable properties that make it preferable to other plasmonic materials like noble metals.[1−4] Researchers have explored its capabilities taking advantage of the long plasmon lifetimes, low losses,[5] high spatial confinement, and versatile tunability,[6,7] together with the large electro-optical response provided by its two-dimensional (2D) geometry and peculiar electronic structure.[8] Graphene-based devices are designed for applications in optoelectronics,[1,9,10] solar cells,[11,12] sensing of gases and molecules,[13−16] photocatalysis,[17,18] THz technology,[19] and so on. Also, the fine biocompatibility of graphene makes it a very good candidate for applications in biotechnology and medical sciences.[20,21] From a fundamental point of view, the simplicity of its atomic structure as well as the definiteness and richness regarding its electronic structure, makes graphene an excellent material to test methods for modeling emerging new phenomena of other low-dimensional systems.[22−24]

Although the optical response of graphene presents collective oscillations at frequencies in the low ultraviolet (UV) range (∼4−30 eV, the so-called π and $\sigma + \pi$ plasmons),[25−28] it is in the terahertz (THz) to infrared (IR)[29] region (with frequencies <1 eV) where it stands out for the aforementioned applications. In this regime, heavily doped graphene supports the so-called Dirac plasmons, originated in intraband π-electron excitations.[30,31] A distinct property of these plasmons is the high tunability of frequencies, which can be controlled by altering the chemical potential through external gates,[6,7] a unique feature not applicable in the higher energy regime. The associated plasmon polariton shows strong confinement in the direction perpendicular to graphene's sheets and propagates along them for relatively long distances.[32] Tunable plasmons have been detected also in a variety of graphene nanostructures, like ribbons, nanodisks, rings, and others,[33] which add localization properties in the plane of the layers. Nevertheless, extended graphene remains a central topic for theoretical as well as experimental investigation, both monolayered and multilayered, isolated or combined with other materials and heterostructures,[5,34−37] and even in nonparallel configurations.[38] Furthermore, stacks of multiple graphene layers, which are typically separated by distances in excess of some 10 nm, have shown great promise for nanophotonic and nanoplasmonic applications due to hybridization taking place

Received: April 1, 2017
Published: July 18, 2017

DOI: 10.1021/acsphotonics.7b00344
ACS Photonics XXXX, XXX, XXX−XXX

between Dirac plasmons in individual layers, which may be tuned by controlling their doping densities.[39−41]

Currently associated with optical spectroscopies and techniques, surface plasmons were first observed in electron energy loss experiments, where energetic free electrons interact with the plasmon fields losing defined amounts of energy.[42,43] Nowadays, electron energy loss spectroscopy (EELS) benefits from the high spatial and energetic resolutions available in transmission electron microscopy (TEM), allowing new insights in the study of plasmons, for example, the mapping of plasmon modes at a nanoscopic scale.[44,45] Also, the experimental setting of a TEM allows for measurements of cathodoluminescence (CL) light emission from the material, which can also be applied to plasmon detection.[46−48] In particular, angle-resolved measurements of CL can be used within TEM experiments to distinguish between transition radiation (TR) and incoherent CL in the form of, for example, luminescence from various materials.[49,50] In addition, a number of experiments have been carried out using different energetic electron sources to generate electromagnetic radiation from graphene,[51−53] increasing the interest in studying the coupling between moving electrons, plasmons, and radiation fields. In that context, electron beam irradiation of graphene has been recently explored for its prospects to fill in technological gap regarding the lack of radiation sources at THz frequencies.[54]

In a recent article,[55] we presented fully relativistic calculations of the energy loss spectra in the THz to UV frequency range, generated by TEM electrons at normal incidence passing through a single layer of graphene. In this paper, we generalize the theoretical framework to multilayer graphene with an arbitrary number of parallel sheets. We assume that graphene layers are well separated so that the only interaction between their electronic systems is due to electromagnetic fields. We solve the corresponding Maxwell equations within the dielectric response formalism with adequate boundary conditions.[56,57] As in the previous work, we elucidate two contributions to the total energy loss of the external particle: the ohmic losses in graphene and the electromagnetic energy emitted in the far field region in the form of TR. We further show that ohmic losses are related to excitation of the Dirac plasmon polaritons (DPPs) in graphene, as well as to generation of the Joule heat due to decay of those DPPs in the presence of dissipative processes in graphene. Focusing on the THz range, we use the Drude model of conductivity and apply our model to double-layer graphene,[39] onto which a ∼100 keV electron beam impinges perpendicularly. We emphasize that we do not consider a bilayer graphene in the sense of two electronically coupled layers.[34]

Besides calculations of the total ohmic and radiative energy loss spectra, we also derive a layer-wise decomposition of the ohmic losses and a directional decomposition of the radiation emitted in the upper and lower half-spaces. Also, relative roles of the bonding and antibonding hybridization modes in the two graphene layers are elucidated by developing a modal decomposition for ohmic losses in the limit of vanishing dissipation in graphene.

Finally, in addition to the case of graphene layers with equal conductivities, we also study an inherently asymmetric structure with two graphene layers having different conductivities due to doping with different densities of charge carriers. We analyze the dependence of the ohmic loss spectra and the angular distribution of the emitted radiation with parameters such as the interlayer distance and the relative doping density.

The paper is organized as follows: in the Theory section, we give a derivation of the electromagnetic fields and define probability densities for various energy losses for the general case of N graphene layers, and apply it to the case of two graphene layers, for which we study a modal decomposition of plasmon excitation probability. The Results and Discussion section is divided in two parts, dedicated to layers with equal conductivities and different conductivities, and is followed by the Conclusions section. Unless otherwise stated, Gaussian units of electrodynamics are used throughout the paper.[58]

THEORY

We consider a structure with N parallel graphene layers with large area placed in the planes $z = z_l$ with $l = 1, 2, ..., N$ in a three-dimensional (3D) Cartesian coordinate system with coordinates $\mathbf{R} = \{\mathbf{r}, z\}$, where $\mathbf{r} = \{x, y\}$, as shown in Figure 1. We assume that the structure is placed in vacuum in order to be able to neglect any other sources of radiation or dissipation, apart from those pertaining to the graphene layers. We find it convenient to use the Hertz vector $\mathbf{\Pi}(\mathbf{R}, t)$,[59] which can be easily obtained by solving a nonhomogeneous Helmholtz equation with an electric current density as source term by means of a free-space, retarded Green's function in scalar form. The background of our formalism was outlined in ref.[55] for single-layer graphene, while some details pertaining to multilayer graphene are given in the Supporting Information (SI) for the present paper.

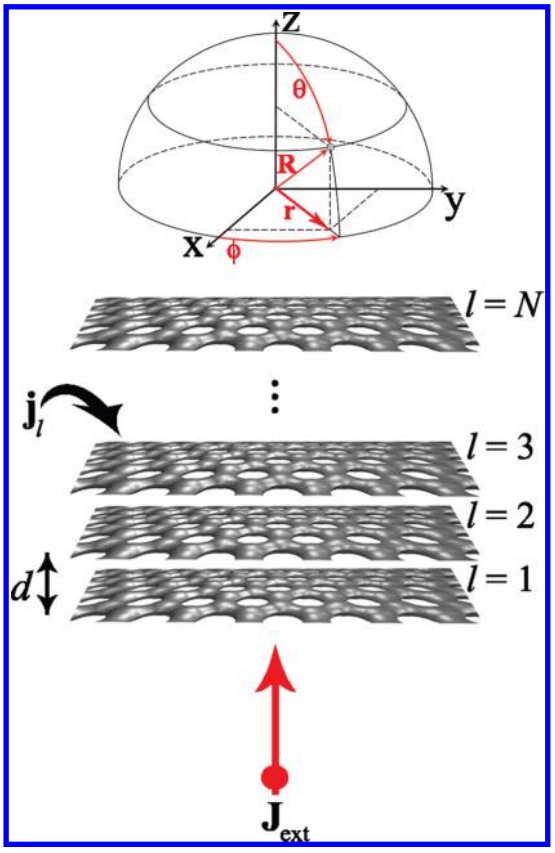

Figure 1. Geometry of the structure for probing the multilayer specimen by an electron in TEM.

General Formulation for *N* Layers. Assuming translational invariance inside each graphene layer, we may perform a two-dimensional (2D) spatial Fourier transform ($\mathbf{r} = \{x, y\} \rightarrow \mathbf{k}$

DOI: 10.1021/acsphotonics.7b00344
ACS Photonics XXXX, XXX, XXX−XXX

$= \{k_x, k_y\}$), as well as a Fourier transform with respect to time ($t \rightarrow \omega$), enabling us to express the Hertz vector as

$$\mathbf{\Pi}(\mathbf{R}, t) = \iint \frac{d^2\mathbf{k}}{(2\pi)^2} e^{i\mathbf{k}\cdot\mathbf{r}} \int_{-\infty}^{\infty} \frac{d\omega}{2\pi} e^{-i\omega t} \mathbf{\Pi}(\mathbf{k}, z, \omega) \tag{1}$$

This vector may be decomposed into two contributions as $\mathbf{\Pi} = \mathbf{\Pi}_{ind} + \mathbf{\Pi}_{ext}$, resulting from the external charged particle and the currents induced in graphene layers, see Figure 1. Considering the external particle to be a point charge Ze that moves along the z axis with constant velocity $\mathbf{v} = \hat{\mathbf{z}}v$ (enabling us to neglect its braking radiation), where $\hat{\mathbf{z}}$ is a unit vector in the direction of that axis, the associated current density, $\mathbf{J}_{ext}(\mathbf{k}, z, \omega) = Zev e^{iz\omega/v}\hat{\mathbf{z}}$, yields the corresponding Hertz vector as $\mathbf{\Pi}_{ext}(\mathbf{k}, z, \omega) = \frac{i}{\omega} A(k, \omega)\mathbf{J}_{ext}(\mathbf{k}, z, \omega)$, with amplitude $A(k, \omega)$ given in the SI. Using standard vector relations, one may retrieve from $\mathbf{\Pi}_{ext}$ the usual expressions for electric and magnetic fields associated with a uniformly moving point charge in free space.[58,59]

Defining $\mathbf{j}_l(\mathbf{k}, \omega)$ as the in-plane current in the lth graphene layer, which arises due to dynamic polarization of charge carriers in that layer, we may express the total induced current in the system in terms of a sum involving Dirac's delta functions as

$$\mathbf{J}_{ind}(\mathbf{k}, z, \omega) = \sum_{l=1}^{N} \delta(z - z_l)\mathbf{j}_l(\mathbf{k}, \omega) \tag{2}$$

We assume that the lth graphene layer is characterized by its own equilibrium density of charge carriers, n_l, giving rise to an in-plane, scalar conductivity $\sigma_l(k, \omega)$, which may be generally dependent on both the wavenumber $k = \sqrt{k_x^2 + k_y^2}$ and frequency ω. Then, the polarization current in that layer may be expressed as $\mathbf{j}_l(\mathbf{k}, \omega) = \sigma_l(k, \omega)\mathbf{E}_{\parallel}(\mathbf{k}, z_l, \omega)$, where $\mathbf{E}_{\parallel}(\mathbf{k}, z_l, \omega)$ is the tangential or the in-plane component of the total electric field evaluated at $z = z_l$. Equation 2 allows us to express the total induced Hertz vector, $\mathbf{\Pi}_{ind}(\mathbf{k}, z, \omega) = \frac{i}{\omega}\frac{2\pi}{q}\sum_{l=1}^{N} e^{-q|z-z_l|}\mathbf{j}_l(\mathbf{k}, \omega)$, which only has components parallel to the graphene layers, as superposition of the longitudinal components of the electric field in the lth layer, $E_l \equiv \hat{\mathbf{k}}\cdot\mathbf{E}_{\parallel}(\mathbf{k}, z_l, \omega)$, where $\hat{\mathbf{k}}$ is a unit vector in the direction of $\mathbf{k}$. A self-consistent set of values for E_l is obtained by solving the system of equations (for a derivation please see eqs S1−S4 in the SI)

$$\left(1 + \frac{2\pi i}{\omega} q\sigma_l\right)E_l + \frac{2\pi i}{\omega} q \sum_{l'=1, l'\neq l}^{N} \sigma_{l'} e^{-q|z_l - z_{l'}|}E_{l'} = \mathcal{A} e^{iz_l\omega/v} \tag{3}$$

where $\mathcal{A} \equiv -ikA\frac{Ze}{v}$ and[55]

$$q(k, \omega) = \begin{cases} \frac{|\omega|}{c}\sqrt{\left(\frac{ck}{\omega}\right)^2 - 1} \equiv \alpha(k, \omega), & |\omega| < ck \\ -i\frac{\omega}{c}\sqrt{1 - \left(\frac{ck}{\omega}\right)^2} \equiv -i\kappa(k, \omega), & |\omega| > ck \end{cases} \tag{4}$$

Here, we have defined α and κ as the inverse decay length of evanescent fields and the wavenumber of radiation in the far-field regions in directions perpendicular to graphene layers, respectively.

Having obtained $\mathbf{\Pi}_{ind}$, one may use standard vector relations to express the induced electric and magnetic fields as[55,59]

$$\mathbf{E}_{ind}(\mathbf{k}, z, \omega) = -\hat{\mathbf{k}}\frac{2\pi i q}{\omega}\sum_{l=1}^{N} \sigma_l e^{-q|z-z_l|}E_l + \hat{\mathbf{z}}\frac{2\pi k}{\omega}\sum_{l=1}^{N} \sigma_l e^{-q|z-z_l|}E_l \mathrm{sign}(z - z_l) \tag{5}$$

$$\mathbf{H}_{ind}(\mathbf{k}, z, \omega) = -\frac{2\pi}{c}(\hat{\mathbf{z}} \times \hat{\mathbf{k}})\sum_{l=1}^{N} \sigma_l e^{-q|z-z_l|}E_l \mathrm{sign}(z - z_l) \tag{6}$$

with "sign" being the signum function.

The energy balance of the system composed of the incident particle traversing a number of graphene layers gives the condition $W_{ext} = W_{ohm} + W_{rad}$, where $W_{ext} > 0$ is the total energy lost by the external charged particle, $W_{ohm} > 0$ is the Joule (or ohmic) energy deposited in the graphene layers, and $W_{rad} > 0$ is the electromagnetic energy radiated in the far field region. We use appropriate physical definitions for each term to deduce expressions for the corresponding probability densities while upholding the conservation of the total energy. Each of those energy contributions may be further suitably decomposed into physically motivated and experimentally observable components.

Invoking the parity property of the Fourier transformed quantities, we may express the total energy loss for each of these channels as the integral

$$W_L = \iint d^2\mathbf{k} \int_0^{+\infty} d\omega \omega F_L(k, \omega) \tag{7}$$

where L = ext, ohm, rad, which defines the corresponding joint probability (or spectral) density $F_L(k, \omega)$ associated with the transfer of energy $\hbar\omega \geq 0$ and the transfer of in-plane momentum $\hbar\mathbf{k}$ from the incident electron to graphene layers.

In the case of ohmic energy losses, the total joint probability density may be written as a layer decomposition, $F_{ohm}(k, \omega) = \sum_{l=1}^{N} F_{ohm,\, l}(k, \omega)$, where $F_{ohm,\, l}(k, \omega)$ describes losses in the lth graphene layer. In the case of radiation energy losses, the total joint probability density may be written as a directional decomposition, $F_{rad}(k, \omega) = F_{rad}^{\uparrow}(k, \omega) + F_{rad}^{\downarrow}(k, \omega)$, where $F_{rad}^{\uparrow\downarrow}(k, \omega)$ describes radiation emitted in the upper half-space ($\uparrow$) and the lower half-space ($\downarrow$).

Any differences between the radiation emitted in the upper and the lower half-spaces would be most feasibly observed in the joint spectral density and the angular distribution, $\mathcal{S}(\theta, \omega)$, defined so that the total radiation energy loss is written as

$$W_{rad} \equiv \iint d^2\hat{\Omega} \int_0^{\infty} d\omega \mathcal{S}(\theta, \omega) \tag{8}$$

where $d^2\hat{\Omega} = \sin\theta d\theta d\phi$ is the element of solid angle in spherical coordinates ($0 \leq \theta \leq \pi$ and $0 \leq \phi < 2\pi$, see Figure 1), with the angle θ defining the direction of radiation with respect to the z axis. One may express the joint spectral density and the angular distribution of radiation as

DOI: 10.1021/acsphotonics.7b00344
ACS Photonics XXXX, XXX, XXX−XXX

$$\mathcal{S}(\theta,\omega)=\frac{\omega^3}{c^2}|\cos\theta| \times\begin{cases} F^{\uparrow}_{\mathrm{rad}}\left(\frac{\omega}{c}\sin\theta,\omega\right), & 0\le\theta\le\pi/2 \\ F^{\downarrow}_{\mathrm{rad}}\left(\frac{\omega}{c}\sin\theta,\omega\right), & \pi/2\le\theta\le\pi \end{cases} \tag{9}$$

In various electron energy loss spectroscopies it is often of interest to study quantities after performing integration over the momentum transfer, so that for each joint probability density function $F_L(k,\omega)$, we define an associated total integrated probability density as

$$P_L(\omega)=\frac{1}{\hbar^2}\iint d^2\mathbf{k}F_L(k,\omega) \tag{10}$$

where L = ext, ohm, rad. In the case of ohmic and radiation losses, one may also express the corresponding integrated densities in terms of layer-wise and directional decompositions, $P_{\mathrm{ohm}}(\omega)=\sum_{l=1}^{N}P_{\mathrm{ohm},\,l}(\omega)$ and $P_{\mathrm{rad}}(\omega)=P^{\uparrow}_{\mathrm{rad}}(\omega)+P^{\downarrow}_{\mathrm{rad}}(\omega)$, respectively.

Two Graphene Layers. We apply the above general formulation of the problem to the case of two parallel graphene layers with distance d between them. Letting $z_{1,2}=\mp\frac{d}{2}$, we solve the system of equations in eq 3 for $E_{1,2}$ and obtain expressions for joint probability densities, which can be shown to verify the conservation of energy in the form $F_{\mathrm{ext}}(k,\omega)=F_{\mathrm{ohm}}(k,\omega)+F_{\mathrm{rad}}(k,\omega)$.

We next show that both the ohmic and the radiative losses exhibit an asymmetry with respect to the direction of motion of the external charge, that is, the corresponding decompositions of those two types of losses depend on the sign of the external charge velocity component along the z axis. This is best illustrated by considering the special case of the symmetric structure consisting of two graphene layers with equal conductivities. In that case, we may write the probability densities for ohmic losses in the layers 1 and 2 as

$$F_{\mathrm{ohm},1,2}(k,\omega)=\frac{|\mathcal{A}|^2}{4\pi^3\omega}\Re\{\sigma\}\left[\frac{1-\cos\left(\frac{\omega}{v}d\right)}{2|\lambda_-|^2}+\frac{1+\cos\left(\frac{\omega}{v}d\right)}{2|\lambda_+|^2}\mp\sin\left(\frac{\omega}{v}d\right)\Im\left\{\frac{1}{\lambda_-^*\lambda_+}\right\}\right] \tag{11}$$

and the probability densities for radiative losses in the upper/lower half-spaces as

$$F^{\uparrow\downarrow}_{\mathrm{rad}}(k,\omega)=\frac{|\mathcal{A}|^2}{4\pi^3\omega}\frac{2\pi}{\omega}\kappa|\sigma|^2\left[\frac{1-\cos\left(\frac{\omega}{v}d\right)}{2|\lambda_-|^2}(1-\cos(\kappa d))+\frac{1+\cos\left(\frac{\omega}{v}d\right)}{2|\lambda_+|^2}(1+\cos(\kappa d))\pm\sin\left(\frac{\omega}{v}d\right)\sin(\kappa d)\Re\left\{\frac{1}{\lambda_-^*\lambda_+}\right\}\right] \tag{12}$$

where $\lambda_{\mp}=1+i\frac{2\pi}{\omega}q\sigma(1\mp e^{-qd})$ are the eigenvalues of a 2×2 matrix, which defines the system of equations in eq 3 upon setting $\sigma_1=\sigma_2=\sigma$. Clearly, asymmetries arise in the layer-wise decomposition of ohmic losses and in the directional decomposition of radiative losses from the last terms in eqs 11 and 12, respectively. Those terms will be canceled out when we evaluate the total ohmic and the total radiative losses as $F_{\mathrm{ohm}}=F_{\mathrm{ohm},1}+F_{\mathrm{ohm},2}$ and $F_{\mathrm{rad}}=F^{\downarrow}_{\mathrm{rad}}+F^{\uparrow}_{\mathrm{rad}}$, respectively.

Going back to a more general case of two graphene layers with different conductivities, $\sigma_1\neq\sigma_2$, we emphasize that the function $F_{\mathrm{rad}}(k,\omega)$ for radiative losses is nonzero only for frequencies above the light line, $\omega>ck$, whereas ohmic losses may generally occur at all frequencies, $\omega>0$. Thus, the function $F_{\mathrm{ohm}}(k,\omega)$ for ohmic losses has nonzero contributions both below and above the light line, which may be accordingly defined via

$$F_{\mathrm{ohm}}(k,\omega)=\begin{cases}F^{<}_{\mathrm{ohm}}(k,\omega), & \omega<ck\\ F^{>}_{\mathrm{ohm}}(k,\omega), & \omega>ck\end{cases} \tag{13}$$

It should be stressed, however, that the probability density $F^{>}_{\mathrm{ohm}}(k,\omega)$ in the second line of the above equation is not associated with any radiation, even though that contribution to ohmic losses covers the region of frequencies above the light line.

Conductivity of each graphene layer has both a dissipative part, $\Re\{\sigma_l\}$, and a reactive part, $\Im\{\sigma_l\}$, which are generally different from zero. While the collective oscillations of charge carriers in each graphene layer or, equivalently, the excitation of its DPP gives rise to $\Im\{\sigma_l\}>0$, scattering of those carriers on phonons, charged impurities or atomic-size defects in graphene gives rise to $\Re\{\sigma_l\}>0$, signaling the existence of several possible decay channels for the DPPs. Referring to the result obtained in the SI, $F_{\mathrm{ohm},l}(k,\omega)=\frac{1}{4\pi^3\omega}|E_l|^2\Re\{\sigma_l\}$, one may assert that the ohmic losses describe both the process of plasmon excitation in graphene layers and the decay of those plasmons, which ultimately generates Joule heat at all frequencies whenever $\Re\{\sigma_l\}>0$.

In an idealized case of clean graphene layers at zero temperature, and at frequencies well separated from the phonon frequencies, it is worthwhile considering a theoretical limit of vanishing dissipation, $\Re\{\sigma_l\}\to 0^+$, when no heat is generated in those layers. It may be then shown that the function in the second line of eq 13 vanishes, $F^{>}_{\mathrm{ohm}}(k,\omega)\to 0$, leaving the radiation to be the only cause of energy losses of the external charged particle at frequencies $\omega>ck$, governed by a probability density $F_{\mathrm{rad}}(k,\omega)$, which turns out to be only marginally affected by reduction of dissipation in graphene layers. On the other hand, it may also be shown that, by taking the limit $\Re\{\sigma_l\}\to 0^+$, the function in the first line of eq 13 does not vanish, but is rather reduced to a new function, $F^{<}_{\mathrm{ohm}}(k,\omega)\to F_{\mathrm{pl}}(k,\omega)$, which we define as the probability density for exciting collective modes that result from hybridization of the DPPs in two graphene layers. In the SI, we outline a procedure showing that, in the limit of vanishing dissipation, $\Re\{\sigma_l\}\to 0^+$, the total probability density of plasmon excitations may be expressed in the form of a modal decomposition, $F_{\mathrm{pl}}(k,\omega)=F^{-}_{\mathrm{pl}}(k,\omega)+F^{+}_{\mathrm{pl}}(k,\omega)$, with the function $F^{\mp}_{\mathrm{pl}}(k,\omega)$ containing a Dirac's delta function that involves a dispersion relation for the bonding/antibonding hybridized mode.

The dispersion relations for those modes may be found by letting $\Re\{\sigma_1\}=\Re\{\sigma_2\}\to 0^+$ in a 2×2 matrix defining the system of equations in eq 3. Solving an eigenvalue problem with that matrix yields two eigenvalues, given by

$$\lambda_{\mp}=1+i\frac{2\pi}{\omega}\alpha\left(\sigma_m\mp\sqrt{\sigma_d^2+\sigma_1\sigma_2e^{-2\alpha d}}\right) \tag{14}$$

DOI: 10.1021/acsphotonics.7b00344
ACS Photonics XXXX, XXX, XXX−XXX

where $\sigma_m = \frac{\sigma_1+\sigma_2}{2}$ and $\sigma_d = \frac{\sigma_2-\sigma_1}{2}$, and $\alpha(k, \omega) \equiv \sqrt{k^2 - \left(\frac{\omega}{c}\right)^2}$. Those eigenvalues have real-valued zeros in the (k, ω) plane only for frequencies below the light line, $0 < \omega < ck$, that is, when $\alpha(k, \omega)$ is real-valued. Note that the square root in eq 14 is purely imaginary in the limit of vanishing dissipation, and it should be taken with the same sign as the sign of the reactive part of graphene conductivities, $\Im\{\sigma_{1,2}\}$. By solving the equations $\lambda_\mp(k, \omega) = 0$, defined via eq 14, we obtain two dispersion relations, $\omega = \omega_\mp(k)$, for two hybridized DPP modes in graphene layers, where the signs $\mp$ correspond to the low-energy bonding and the high-energy antibonding coupling between the layers, respectively.[39,40] Since those dispersion relations are located below the light line, excitation of long-lived bonding and antibonding DPP modes is the only cause of energy losses of the external charged particle at frequencies $\omega < ck$ in the limit of vanishing dissipation in graphene, governed by the probability density $F_{\text{pl}}(k, \omega)$.

We note that our theory may be implemented for any 2D material, which can be described by a scalar conductivity $\sigma(k, \omega)$. In order to be specific, we adopt here a Drude model for optical conductivity of doped graphene, but note that conclusions of this work are applicable to any 2D conductive system exhibiting low-energy intraband electronic excitations that may be described by a Drude-type model.[31] Our interest in doped graphene stems from the fact that it supports the technologically interesting Dirac plasmon in the THz to IR frequency range,[19] which is well reproduced by the Drude model.[3] At the same time, this range of frequencies implies that we work in an extreme long-wavelength limit, for which Novko et al. showed that ab initio calculations of graphene conductivity give a Drude model as correct $k \to 0$ limit at low frequencies.[60] We further assume that distances between graphene layers in our work are large enough that the electronic band structure of each layer is not affected by the presence of other layers, so that the optical conductivity of each layer may be adequately described by a Drude model under sufficient graphene doping.[41] The validity of this assumption was demonstrated in experiments performed by Yan et al. on the IR plasmonic devices with stacks of graphene layers separated by 20 nm thick spacers.[40]

Drude model for optical conductivity of the lth graphene layer, with $l = 1, 2$, is given by

$$\sigma_l(\omega) = i\frac{v_{\text{B}}}{\pi}\frac{v_{\text{F}}k_{\text{F},l}}{\omega + i\gamma_l} \tag{15}$$

where $v_{\text{B}} = e^2/\hbar \approx c/137$ is the Bohr velocity with c being the speed of light, $v_{\text{F}} \approx c/300$ is the Fermi speed of graphene's π electron bands, $k_{\text{F},l} = \sqrt{\pi|n_l|}$ is the Fermi wavenumber in the lth graphene layer, and γ_l is phenomenological damping rate, which we let $\gamma_l \to 0^+$ in the limit of vanishing dissipation.

It is convenient to introduce reduced wavenumber and reduced frequency, $\overline{k} = k/k_c$ and $\overline{\omega} = \omega/\omega_c$, respectively.[55] In the case of two graphene layers, we define $k_c = v_{\text{B}}v_{\text{F}}(k_{\text{F},1} + k_{\text{F},2})/(2c^2)$ and $\omega_c = ck_c$. For typical doping densities in graphene layers, $|n_l| \sim 10^{13}$ cm^{-2}, we obtain $k_c \sim 1.36 \times 10^{-5}$ nm^{-1} and $\omega_c/(2\pi) \sim 0.65$ THz. The system also needs to be characterized by the ratio $\rho = k_{\text{F},1}/k_{\text{F},2}$, where $l = 1$ stands for the "lower" layer and $l = 2$ stands for the "upper" layer with respect to the direction of the z axis. Thus, defining the reduced conductivities by $\overline{\sigma}_l = \sigma_l/c$, we may write

$$\overline{\sigma}_1(\overline{\omega}) = \frac{i}{\pi}\frac{2\rho}{\rho+1}\frac{1}{\overline{\omega} + i\overline{\gamma}_1} \quad \text{and} \quad \overline{\sigma}_2(\overline{\omega}) = \frac{i}{\pi}\frac{2}{\rho+1}\frac{1}{\overline{\omega} + i\overline{\gamma}_2} \tag{16}$$

where $\overline{\gamma}_l = \gamma_l/\omega_c$ are the reduced damping rates.

Upon switching to reduced units and setting $\overline{\gamma}_1 = \overline{\gamma}_2 = 0$ in eq 16, it may be shown that the equations $\lambda_\mp(k, \omega) = 0$ become equivalent to $\overline{\omega}^2 - 2\overline{\alpha}[1 \mp \mathcal{R}(\overline{\alpha})] = 0$, where $\overline{\alpha} = \sqrt{\overline{k}^2 - \overline{\omega}^2}$ and

$$\mathcal{R}(\overline{\alpha}) = \sqrt{\left(\frac{\rho-1}{\rho+1}\right)^2 + \frac{4\rho e^{-2\overline{\alpha}\overline{d}}}{(\rho+1)^2}} \tag{17}$$

with $\overline{d} = k_c d$. Solving those equations in the region below the light line, $0 < \overline{\omega} < \overline{k}$, gives the dispersion relations of the bonding/antibonding modes in reduced units, $\overline{\omega} = \overline{\omega}_\mp(\overline{k})$.

Finally, we obtain the probability densities of exciting the bonding and antibonding modes as

$$F_{\text{pl}}^{\mp} = F_c\frac{\beta^2(\overline{\omega}^2 + \overline{\alpha}^2)}{(\overline{\omega}^2 + \overline{\alpha}^2\beta^2)^2}\left\{1 \mp \frac{1}{\mathcal{R}(\overline{\alpha})}\left[\left(\frac{\rho-1}{\rho+1}\right)^2 + \frac{4\rho e^{-\overline{\alpha}\overline{d}}}{(\rho+1)^2}\cos\left(\frac{\overline{\omega}}{\beta}\overline{d}\right)\right]\right\} \times \delta(\overline{\omega}^2 - 2\overline{\alpha}[1 \mp \mathcal{R}(\overline{\alpha})]) \tag{18}$$

where $F_c \equiv 4(Ze)^2/(\pi\omega_c^2 k_c)$ and $\beta \equiv v/c$. As with the other contributions to energy losses, we may use the above result in eq 10 to define the integrated probability densities, $P_{\text{pl}}^{\mp}(\omega)$, for exciting the bonding and antibonding modes per unit interval of frequency. Note that integration of $F_{\text{pl}}^{\mp}(\overline{k}, \overline{\omega})$ over $\overline{k}$ (or $\overline{\alpha}$) is greatly aided by the presence of the Dirac's δ function in eq 18, which is peaked along the dispersion relation $\overline{\omega} = \overline{\omega}_\mp(\overline{k})$ for those two modes.

RESULTS AND DISCUSSION

While the formalism developed in the preceding section can be directly applied to multiple layers of any 2D material described by a scalar conductivity,[61] it may also be readily generalized to anisotropic 2D materials.[62] However, we are primarily interested in graphene based layered structures of interest for possible applications in photonic and plasmonic devices that operate in the THz to IR range of frequencies. For this purpose it suffices to adopt the Drude model in eq 15, which is accurate enough for doped graphene satisfying $k \ll \omega/v_{\text{F}} \ll k_{\text{F}}$,[31] or in terms of the reduced variables, $\frac{v_{\text{F}}}{c}\overline{k} \ll \overline{\omega} \ll \frac{c}{v_{\text{B}}}$.[55]

For two graphene layers, one of the most important parameters is the interlayer distance d, which we define in reduced units as $\overline{d} = k_c d$ and take it to vary in the range of values $10^{-3} \le \overline{d} \le 1$, corresponding to 73 nm $\lesssim d \lesssim$ 73 μm for doping densities of $|n_l| = 10^{13}$ cm^{-2}. At such large distances, one may neglect the electron hopping between neighboring graphene layers, as well as the effects of static electric field between differently doped graphene layers due to potential bias between them. Hence, the electronic structure of each graphene layer is treated as independent from other layers, and the only interaction between them is due to electromagnetic fields.

Our calculations are designed to illustrate interferences due to retardation effects, which may give rise to asymmetries in (a) directional decomposition of the radiation emitted in the upper and lower half-spaces, (b) layer-wise decomposition of the ohmic losses in graphene, and (c) modal decomposition of the plasmon excitation probability density for the bonding and antibonding modes. We analyze what roles are played in those

DOI: 10.1021/acsphotonics.7b00344
ACS Photonics XXXX, XXX, XXX−XXX

interference effects by the distance d and the ratio $\rho = k_{F,1}/k_{F,2} = \sqrt{|n_1|/|n_2|}$ defining asymmetry between the doping densities of the two graphene layers.

At the same time, we keep the damping rates in graphene layers fixed at a given value $\overline{\gamma}_l = 0.1$, except when discussing the dispersion relations of hybridized DPP modes and the corresponding modal decomposition. In addition, we assume the external particle to be an electron ($Z = 1$) and keep its (reduced) speed fixed at the value $\beta = v/c = 0.5$, corresponding to a typical electron velocity in TEM. The effects of variation in the $\overline{\gamma}_l$ and β values are illustrated in the SI.

Equal Conductivities. In this subsection, we study the case of two graphene layers with equal doping densities ($\rho = 1$) and, hence, equal conductivities, $\sigma_1 = \sigma_2 = \sigma(\omega)$, described by the Drude's model in eq 15.

In Figure 2, we show the joint probability densities for (a) ohmic losses, $\overline{F}_{ohm}(\overline{k}, \overline{\omega})$, and (b) radiation losses, $\overline{F}_{rad}(\overline{k}, \overline{\omega})$, as functions of the reduced frequency and wavenumber, $\overline{\omega}$ and $\overline{k}$, for an illustrative case of the reduced interlayer distance $\overline{d} = 0.1$. The color coding for those functions is based on reduced units

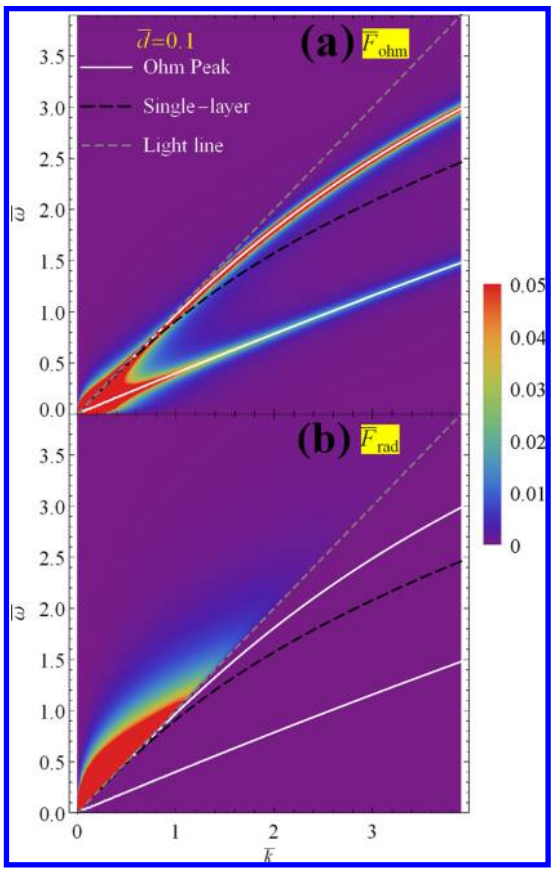

Figure 2. (a) The total ohmic, $\overline{F}_{ohm}(\overline{k}, \overline{\omega})$, and (b) the total radiative, $\overline{F}_{rad}(\overline{k}, \overline{\omega})$, joint probability densities for two graphene layers having equal conductivities with the damping rate $\overline{\gamma} = 0.1$, for interlayer distance $\overline{d} = 0.1$, and the reduced electron speed $\beta \equiv v/c = 0.5$. Results are shown in reduced units using the normalization factor $F_c = 4(Ze)^2/(\pi\omega_c^2 k_c)$. Also shown are the dispersion relations for the bonding and antibonding modes with eigenfrequencies $\overline{\omega}_{\mp}(\overline{k})$ for two graphene layers (white solid lines), the dispersion curve for single graphene layer (black dashed line) with eigenfrequency $\overline{\omega}_{single} = \sqrt{2(-1 + \sqrt{1 + \overline{k}^2})}$, and the light line (gray dashed line) $\overline{\omega} = \overline{k}$.

using the normalization factor $F_c = 4e^2/(\pi\omega_c^2 k_c)$. Also shown are the dispersion relations for the bonding and antibonding modes with eigenfrequencies $\overline{\omega}_{\mp}(\overline{k})$ for two graphene layers (white solid lines), the dispersion curve for single graphene layer (black dashed line) with eigenfrequency $\overline{\omega}_{single} = \sqrt{2(-1 + \sqrt{1 + \overline{k}^2})}$ and the light line (gray dashed line) $\overline{\omega} = \overline{k}$. One notices that, in general, $\overline{\omega}_- < \overline{\omega}_{single} < \overline{\omega}_+$, as a consequence of the DPP hybridization for finite $\overline{d}$, whereas $\overline{\omega}_+ < \overline{k}$ as a consequence of retardation effects. While for $\overline{d} \to \infty$ we expect that $\overline{\omega}_{\mp} \to \overline{\omega}_{single}$, the separation between $\overline{\omega}_{\mp}$ increases with decreasing interlayer distance. In the long wavelength limit, when $kd = \overline{k}\overline{d} \ll 1$, we find for antibonding mode $\overline{\omega}_+ \approx 2\sqrt{-2 + \sqrt{4 + \overline{k}^2}}$, corresponding to a single graphene layer with doubled Fermi wavenumber. On the other hand, the bonding mode frequency attains a quasi-acoustic dispersion $\overline{\omega}_- \approx \sqrt{\frac{2\overline{d}}{1 + 2\overline{d}}}\,\overline{k}$, which is not affected by retardation effects for small intergraphene distances, $\overline{d} \ll 1$. Dispersion relations are studied in some detail in the SI, where it is observed that, generally, the bonding mode frequency $\overline{\omega}_-(\overline{k})$ is much more affected by variations in the interlayer distance $\overline{d}$ than the antibonding mode frequency $\overline{\omega}_+(\overline{k})$.

It is obvious from the panel (a) of Figure 2 that the peak values of $\overline{F}_{ohm}(\overline{k}, \overline{\omega})$ closely follow the dispersion curves for bonding and antibonding DPP modes, indicating that ohmic energy losses of the external electron mostly go to excitations of those modes. However, the finiteness of $\overline{\gamma}$ causes a significant fraction of ohmic losses to go to generating Joule heat in the layers, as is indicated by the red regions below and above the light line in Figure 2a, around small $\overline{\omega}$ and $\overline{k}$ values. When the damping rate is reduced, the energy losses due to the Joule heating are reduced, leaving the excitation of long-lived bonding and antibonding DPP modes as the only contribution to the ohmic losses in the limit $\gamma \to 0^+$. In that limit, $\overline{F}_{ohm}(\overline{k}, \overline{\omega})$ in Figure 2a would be represented by a weighted superposition of two Dirac's delta functions located at the dispersion relations $\overline{\omega} = \overline{\omega}_{\mp}(\overline{k})$. On the other hand, in the panel (b) of Figure 2 one notices that $\overline{F}_{rad}(\overline{k}, \overline{\omega})$ exhibits a relatively broad spectrum of radiation energy losses, which are strictly located above the light line, $\overline{\omega} > \overline{k}$. Those losses are not strongly affected by reduction of the damping rate, and they remain finite in the limit of vanishing dissipation in graphene.

Changing the interlayer distance $\overline{d}$ brings rich variety of effects due to retardation in both the dispersion relations $\overline{\omega} = \overline{\omega}_{\mp}(\overline{k})$, and the probability densities $\overline{F}_{ohm}(\overline{k}, \overline{\omega})$ and $\overline{F}_{rad}(\overline{k}, \overline{\omega})$. Figure 3 shows such effects in the radiation spectra, which should be readily observable by using angle-resolved measurements of TR of double-layer graphene in TEM.[47,49,50] In this figure, the angular distribution of the joint spectral density of radiation emitted from two graphene layers, $\overline{\mathcal{S}}(\theta, \overline{\omega})$, is plotted as a function of the angle θ relative to the direction of motion of the external electron, for several values of the radiation frequency $\overline{\omega}$. Results are shown using reduced units for the spectral density with normalization factor $\mathcal{S}_c = e^2/c$, for two interlayer distances, (a) $\overline{d} = 0.1$ and (b) $\overline{d} = 1$. One sees typical "butterfly" patterns of TR, with no noticeable difference between contributions to the upper and lower half-spaces for the shorter distance $\overline{d} = 0.1$, similar to the case of single-layer graphene.[55] On the other hand, there is quite large asymmetry between the angular distributions of radiation emitted in the upper and lower half-spaces at the longer distance $\overline{d} = 1$, which

DOI: 10.1021/acsphotonics.7b00344
ACS Photonics XXXX, XXX, XXX−XXX

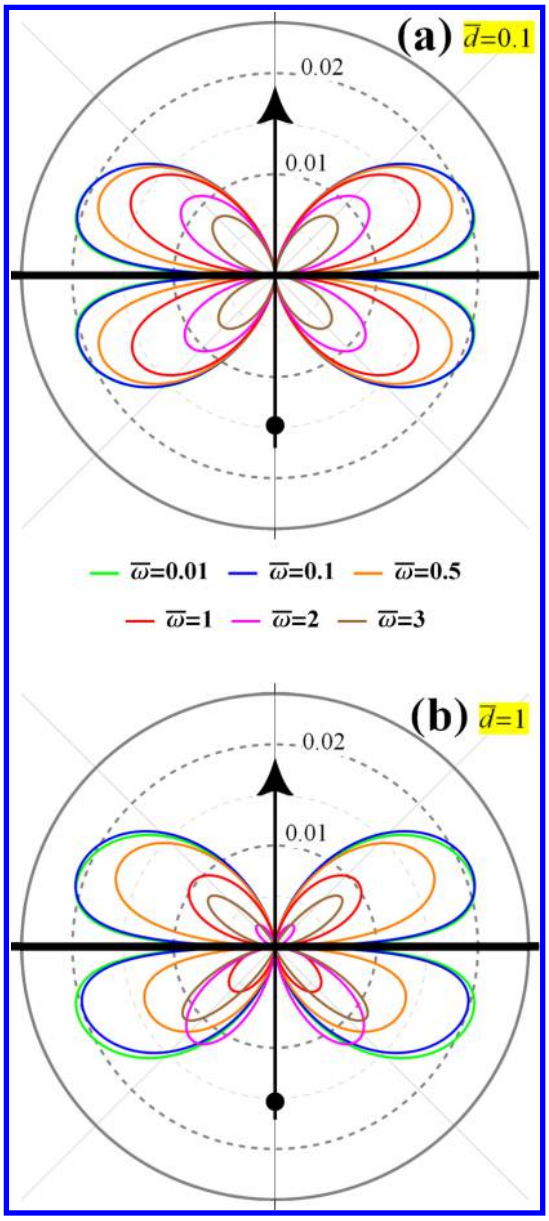

Figure 3. Angular joint probability density $\overline{\mathcal{S}}(\theta, \overline{\omega})$, normalized using the factor $\mathcal{S}_c = (Ze)^2/c$, for two graphene layers having equal conductivities with the damping rate $\overline{\gamma} = 0.1$, for the reduced electron speed $\beta = 0.5$, and for two interlayer distances: (a) $\overline{d} = 0.1$ and (b) $\overline{d} = 1$, and for several reduced frequencies $\overline{\omega}$. A strong directional asymmetry arises between the radiation emitted in the upper and lower half-spaces for the larger interlayer distance.

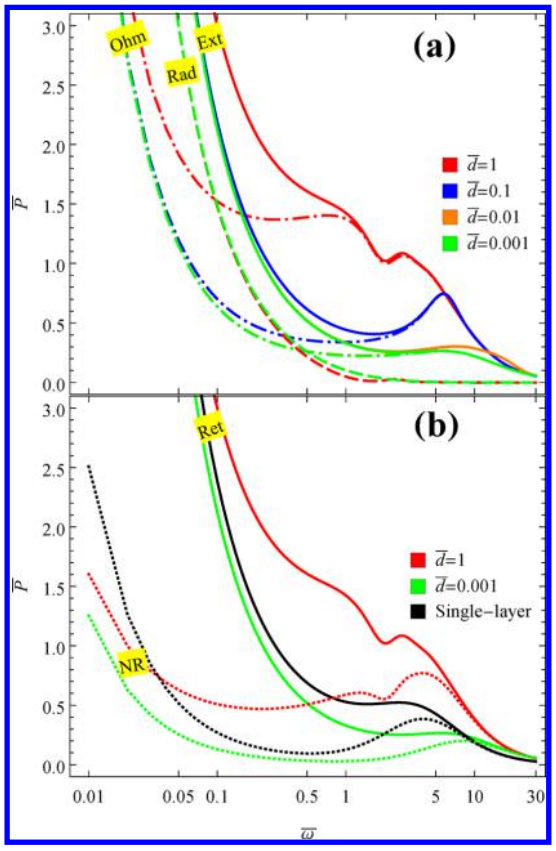

Figure 4. (a) Integrated probability density $\overline{P}$ is shown in reduced units using the normalization factor $P_c = \frac{4}{\pi}\frac{v_B}{c}\frac{1}{\hbar\omega_c}$ as a function of the reduced frequency $\overline{\omega}$ for the total energy loss of the external charged particle, $\overline{P}_{ext}(\overline{\omega})$ (solid lines), the total ohmic loss, $\overline{P}_{ohm}(\overline{\omega})$ (dot-dashed lines), and the total radiative loss, $\overline{P}_{rad}(\overline{\omega})$ (dashed lines) for several interlayer distances, $\overline{d}$ = 1, 0.1, 0.01, and 0.001. (b) The results for $\overline{P}_{ext}(\overline{\omega})$ in two graphene layers at the distances $\overline{d}$ = 0.001 and 1, as well as those for $\overline{P}_{ext}(\overline{\omega})$ in single graphene layer (solid lines) are compared with the corresponding results obtained in the nonretarded limit (dotted lines). For both panels: $\overline{\gamma}$ = 0.1 and β = 0.5.

is particularly emphasized with increasing frequencies. This asymmetry results from the interference terms in eq 12, which contain the factor $\sin(\omega d/v)\sin(\kappa d) = \sin(\overline{\omega}\overline{d}/\beta)\sin(\overline{\omega}\overline{d}\cos(\theta))$, explaining the retardation origin of the asymmetry, as well as why the asymmetry is diminished when $\overline{\omega}\overline{d} \ll 1$. Further discussion of the effects of changing $\overline{d}$ is included in SI.

In the panel (a) of Figure 4 we show the integrated probability densities for the total energy loss of the external electron, $\overline{P}_{ext}(\overline{\omega})$ (solid lines), total ohmic loss, $\overline{P}_{ohm}(\overline{\omega})$ (dash-dotted lines), and the total radiation loss, $\overline{P}_{rad}(\overline{\omega})$ (dashed lines). Results are displayed in reduced units using the normalization factor $P_c = \frac{4}{\pi}\frac{v_B}{c}\frac{1}{\hbar\omega_c}$, for several values of the intergraphene distance in the interval $0.001 \leq \overline{d} \leq 1$. While those three functions were computed from their respective definitions, we remark that each set of curves in Figure 4(a) upholds the conservation of energy in the sense $\overline{P}_{ext}(\overline{\omega}) = \overline{P}_{ohm}(\overline{\omega}) + \overline{P}_{rad}(\overline{\omega})$. One notices that $\overline{P}_{ext}(\overline{\omega})$ is almost completely determined by the ohmic losses $\overline{P}_{ohm}(\overline{\omega})$ for frequencies $\overline{\omega} > 1$, where the main channel of the total energy loss of the external charged particle is due to excitation of the hybridized DPP modes, see Figure 2. On the other hand, radiation losses $\overline{P}_{rad}(\overline{\omega})$ are comparable to the ohmic losses when $\overline{\omega} \sim 1$, and they become a dominant contribution to $\overline{P}_{ext}(\overline{\omega})$ for $\overline{\omega} \lesssim 0.1$.

It is interesting to see in Figure 4a that there is almost no dependence on the interlayer distance in radiation losses, $\overline{P}_{rad}(\overline{\omega})$, indicating that integration of the angular distributions shown in Figure 3 over a full range of angles $0 \leq \theta \leq \pi$ removes the dependence on $\overline{d}$. This may be traced to the presence of factors $[1 \mp \cos(\kappa d)]$ in eq 12, which exhibit strong oscillations as functions of κ (and k) for large d values. When integration over k is performed in $F_{rad}(k, \omega)$ to obtain $P_{rad}(\omega)$, then the d-dependence that would result from the nearby factors $[1 \mp \cos(\omega d/v)]$ in eq 12 is washed out. On the other hand, the integrated ohmic losses in Figure 4a, $\overline{P}_{ohm}(\overline{\omega})$, show rather strong dependence on the interlayer distance in the range $\overline{d} \geq$

DOI: 10.1021/acsphotonics.7b00344
ACS Photonics XXXX, XXX, XXX−XXX

0.1. This may be explained by absence of any factors exhibiting strong oscillations as a function of k in eq 11. Then, the factors $[1 \mp \cos(\omega d/v)]$, which are present in that equation, survive integration over k in $F_{ohm}(k, \omega)$, giving rise to strong interference effects in the resulting distribution of ohmic losses $P_{ohm}(\omega)$ for two graphene layers at a large distance.

In the panel (b) of Figure 4, we compare the results for $\overline{P}_{ext}(\overline{\omega})$, including retarded effects with the nonretarded case, $\overline{P}_{ext}^{NR}(\overline{\omega}) \equiv \overline{P}_{ohm}^{NR}(\overline{\omega})$ (discussed in the SI), for two graphene layers at the distances $\overline{d} = 0.001$ and $\overline{d} = 1$, as well as for a single graphene layer. One sees that the effects of retardation are quantitatively relevant for ohmic losses at frequencies $\overline{\omega} < 10$, giving rise to a significant increase in magnitude of $\overline{P}_{ohm}(\overline{\omega})$ in comparison to $\overline{P}_{ohm}^{NR}(\overline{\omega})$. When combined with the radiation losses, this increase amounts to $\overline{P}_{ext}(\overline{\omega}) \gg \overline{P}_{ext}^{NR}(\overline{\omega})$ for $\overline{\omega} \lesssim 1$. On the other hand, one sees in Figure 4b that the results for two graphene layers with short separation of $\overline{d} = 0.001$ exhibit energy losses that are quite similar to those for single graphene layer, both in the retarded and nonretarded cases, whereas two layers with larger separation of $\overline{d} = 1$ exhibit substantially larger energy losses in both cases.

From Figure 4, one may conclude that interesting interference effects arise in the ohmic losses of two graphene layers at large distances. For example, a curious peak-and-valley structure develops in $\overline{P}_{ohm}(\overline{\omega})$ in the retarded case for $\overline{d} = 1$ in the interval of frequencies $1 \lesssim \overline{\omega} \lesssim 5$, which degenerates in a structure with two peaks in the nonretarded case. Hence, it is worthwhile analyzing separate ohmic losses in each graphene layer. In addition, recalling the strong asymmetries observed in Figure 3b for $\overline{d} = 1$ at higher frequencies, it appears also worthwhile analyzing the angle-integrated energy losses due to radiation emitted in the upper and the lower half-spaces. Accordingly, we show in Figure 5 the integrated probability density of the total energy loss of the external electron, $\overline{P}_{ext}(\overline{\omega})$, along with the layer-wise decomposition of the integrated probability density for ohmic losses in the lower and upper graphene layers, $\overline{P}_{ohm,1}(\overline{\omega})$ and $\overline{P}_{ohm,2}(\overline{\omega})$, and the directional decomposition of the integrated probability density for radiation losses in the upper and lower half-spaces, $\overline{P}_{rad}^{\uparrow}(\overline{\omega})$ and $\overline{P}_{rad}^{\downarrow}(\overline{\omega})$, for two interlayer distances, (a) $\overline{d} = 1$ and (b) $\overline{d} = 0.1$.

It is interesting to see in Figure 5 that there is almost no asymmetry between $\overline{P}_{rad}^{\uparrow}(\overline{\omega})$ and $\overline{P}_{rad}^{\downarrow}(\overline{\omega})$, which are obtained by integrating the angular distributions shown in Figure 3 over two ranges of angles, $0 \le \theta \le \pi/2$ and $\pi/2 \le \theta \le \pi$, respectively. The fact that the asymmetry seen in the angular distributions shown in Figure 3b for $\overline{d} = 1$ has disappeared upon integration may be traced to the same reason as the lack of dependence on the interlayer distance $\overline{d}$ in the total radiative losses, $\overline{P}_{rad}(\overline{\omega}) = \overline{P}_{rad}^{\uparrow}(\overline{\omega}) + \overline{P}_{rad}^{\downarrow}(\overline{\omega})$. Namely, the presence of the factor $\sin(\kappa d)$ in the interference terms in eq 12 gives rise to strong oscillations as a function of κ (and k), which will largely diminish contributions of those terms upon integration of $\overline{F}_{rad}^{\uparrow\downarrow}(k, \overline{\omega})$ over k.

On the other hand, one sees in Figure 5 that $\overline{P}_{ohm,1}(\overline{\omega})$ and $\overline{P}_{ohm,2}(\overline{\omega})$ exhibit relatively large differences for $\overline{\omega} \lesssim 1$ with increasing $\overline{d}$ values, resulting from the interference terms with the factor $\sin(\omega d/v)$ in eq 11, which survives integration of $F_{ohm,1,2}(k, \omega)$ over k. It is interesting that $\overline{P}_{ohm,2}(\overline{\omega}) < \overline{P}_{ohm,1}(\overline{\omega})$ at $\overline{\omega} \lesssim 1$ for both interlayer distances in Figure 5, showing that lower graphene layer absorbs more ohmic losses than the upper layer at low frequencies. Moreover, there are some other interesting features in ohmic losses of individual graphene

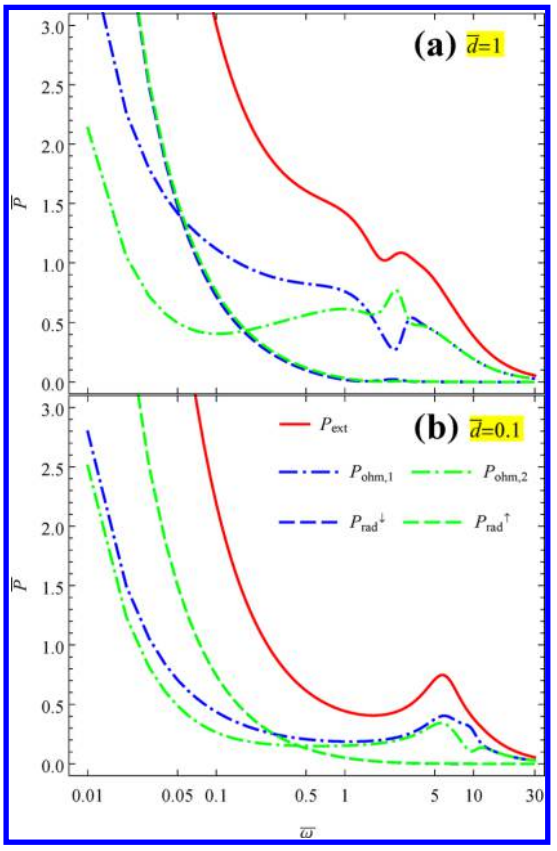

Figure 5. Layer-wise decomposition of the integrated ohmic energy losses, $\overline{P}_{ohm,1,2}(\overline{\omega})$, and a directional decomposition of the integrated radiative losses, $\overline{P}_{rad}^{\uparrow\downarrow}(\overline{\omega})$, are shown in reduced units for two graphene layers at the distances: (a) $\overline{d} = 1$ and (b) $\overline{d} = 0.1$. The ohmic decomposition (dot-dashed lines) shows strong asymmetry with respect to the direction of motion for increasing $\overline{d}$, while the radiation decomposition (dashed lines) shows no such asymmetry. Also shown are the results for the total integrated energy loss of the external charged particle, $\overline{P}_{ext}(\overline{\omega})$ (solid lines). All results are obtained with $\overline{\gamma} = 0.1$ and $\beta = 0.5$.

layers at high frequencies, $\overline{\omega} \gtrsim 1$. For example, it appears that the peak-and-valley structure seen in $\overline{P}_{ext}(\overline{\omega})$ in the interval of frequencies $1 \lesssim \overline{\omega} \lesssim 5$ in Figure 5a for $\overline{d} = 1$ results from partial cancelation of a local minimum in $\overline{P}_{ohm,1}(\overline{\omega})$ and a local maximum in $\overline{P}_{ohm,2}(\overline{\omega})$. This effect also explains the double-peak structure seen in the total ohmic loss, $\overline{P}_{ohm}(\overline{\omega}) = \overline{P}_{ohm,1}(\overline{\omega}) + \overline{P}_{ohm,2}(\overline{\omega})$, in Figure 4a for $\overline{d} = 1$. Likewise, even though $\overline{P}_{ext}(\overline{\omega})$ exhibits a single peak near $\overline{\omega} = 5$ in Figure 5b for $\overline{d} = 0.1$, ohmic losses of individual layers, $\overline{P}_{ohm,1,2}(\overline{\omega})$, show somewhat unexpected features at frequencies $\overline{\omega} > 5$.

In the SI, we show that dominant contributions to the joint probability densities for ohmic losses in both the lower and upper graphene layers, $\overline{F}_{ohm,1}(\overline{k}, \overline{\omega})$ and $\overline{F}_{ohm,2}(\overline{k}, \overline{\omega})$, are contained in two peak regions centered at the frequencies $\overline{\omega}_{\mp}$ corresponding to the bonding and antibonding DPP modes. Relative weights describing the participation of these modes in the ohmic losses in each graphene layer strongly depend on the interlayer distance d. Accordingly, it is worthwhile to take the limit of vanishing damping rates in graphene layers and to evaluate the modal decomposition of the integrated probability density for ohmic energy losses in both graphene layers. Such decomposition gives the probability densities, $\overline{P}_{pl}^{-}(\overline{\omega})$ and $\overline{P}_{pl}^{+}(\overline{\omega})$, for exciting the bonding and antibonding DPP modes per unit frequency, respectively. As a result, we reveal below in

DOI: 10.1021/acsphotonics.7b00344
ACS Photonics XXXX, XXX, XXX−XXX

Figure 6 that oscillations arise in the modal decomposition, which may shed light on the features observed at large

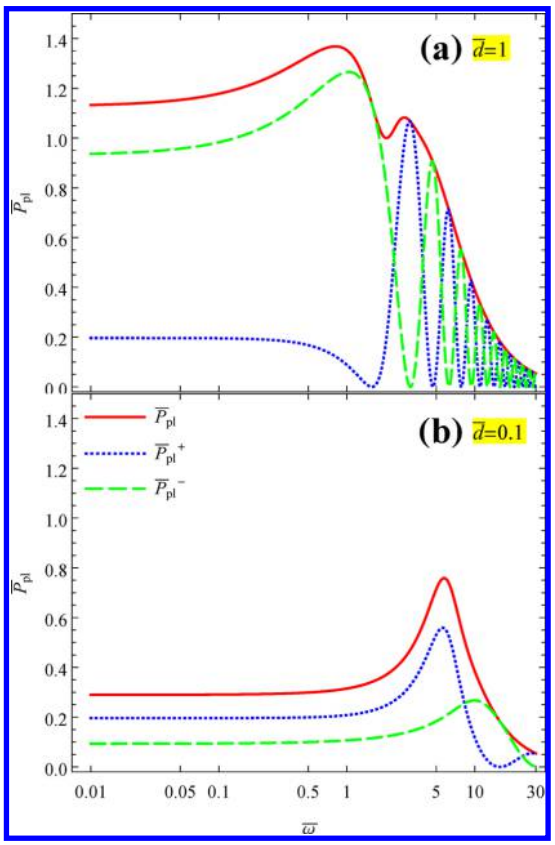

Figure 6. Modal decomposition of the integrated probability density for plasmon polariton excitations in two graphene layers having equal conductivities with zero damping, $\bar{\gamma} = 0$, for two interlayer distances: (a) $\bar{d} = 1$ and (b) $\bar{d} = 0.1$. The reduced speed of the external electron is $\beta = 0.5$. The blue dotted lines label excitations of the bonding and the green dashed lines label excitations of the antibonding modes, while the red solid lines show the total excitation probabilities.

frequencies in the total ohmic losses $\bar{P}_{ohm}(\bar{\omega})$ in Figure 4, and in their layer components $\bar{P}_{ohm,\,1,\,2}(\bar{\omega})$ in Figure 5.

In Figure 6 we show the modal decomposition of the probability density for plasmon excitations, $\bar{P}_{pl}(\bar{\omega}) = \bar{P}_{pl}^{-}(\bar{\omega}) + \bar{P}_{pl}^{+}(\bar{\omega})$, for (a) $\bar{d} = 1$ and (b) $\bar{d} = 0.1$. Results are shown in reduced units using the normalization factor $P_c = \frac{4}{\pi}\frac{v_B}{c}\frac{1}{\hbar\omega_c}$. One notices strong oscillations in the components $\bar{P}_{pl}^{\mp}(\bar{\omega})$ at large frequencies, which nevertheless superimpose into a rather smooth frequency dependence of the total probability density for plasmon excitation, $\bar{P}_{pl}(\bar{\omega})$, in that range. The origin of these oscillations may be explained by setting $\rho = 1$ in the expressions within curly brackets in eq 18, giving factors $1 \mp \cos(\omega d/v) = 1 \mp \cos(\bar{\omega}\,\bar{d}/\beta)$, which survive upon integrating $F_{pl}^{\mp}(k, \omega)$ over k to obtain $P_{pl}^{\mp}(\omega)$. The onset of these oscillations around the frequency $\bar{\omega} \sim \pi\beta/\bar{d}$ seems to give rise to the features observed in ohmic losses at high frequencies in Figure 5. For example, referring to Figure 6a, one may ascertain that the double peak seen in $\bar{P}_{ohm}(\bar{\omega})$ in Figure 4a for $\bar{d} = 1$, which is a result of coupling of the external electron to the bonding and antibonding modes, is accompanied by an interference that gives rise to the peak-and-valley structure seen in $\bar{P}_{ext}(\bar{\omega})$ in Figures 4a and 5a for $\bar{d} = 1$. On the other hand, referring to Figure 6b, one may ascertain that the main peak seen near $\bar{\omega} = 5$ in both $\bar{P}_{ext}(\bar{\omega})$ and $\bar{P}_{ohm}(\bar{\omega})$ in Figure 4a for $\bar{d} = 0.1$ predominantly originates from the antibonding mode, whereas features seen in $\bar{P}_{ohm,1,2}(\bar{\omega})$ at $\bar{\omega} > 5$ in Figure 5b for $\bar{d} = 0.1$ are the signature of interferences between the bonding and antibonding modes.

By comparison of $\bar{P}_{pl}(\bar{\omega})$ in Figure 6 with the function $\bar{P}_{ohm}(\bar{\omega})$ for $\bar{d} = 1$ and 0.1 in Figure 4a, one may assert that the total integrated ohmic losses at frequencies $\bar{\omega} \gtrsim 1$ are dominated by the excitation of both the bonding and antibonding DPP modes. Further comparison reveals that the plasmon excitation probability densities in Figure 6 approach constant values at low frequencies, $\bar{\omega} < 1$, in contrast to the behavior of the ohmic losses in Figures 4 and 5, which grow in magnitude with decreasing $\bar{\omega}$. This difference is a consequence of the fact that the integrated probability densities for ohmic losses in Figures 4 and 5 were calculated with finite damping rate of $\bar{\gamma} = 0.1$, whereas the plasmon excitation probability densities in Figure 6 are calculated in the limit of vanishing damping rates. Accordingly, the competition between the ohmic and radiation losses seen in Figures 4 and 5 at frequencies $\bar{\omega} \lesssim 1$ is strongly affected by increasing the damping rates in graphene layers, which ultimately leads to deposition of the Joule heat in those layers at such frequencies, as discussed in Figure 2.

Finally, regarding the role of the interlayer distance in Figure 6, it is interesting to note that $\bar{P}_{pl}^{-}(\bar{\omega})$ and $\bar{P}_{pl}^{+}(\bar{\omega})$ settle at different constant values at low frequencies, $\bar{\omega} < 1$. In particular, the probability density of exciting the antibonding mode at such frequencies, $\bar{P}_{pl}^{+} \approx 0.2$, is not affected by the value of $\bar{d}$, whereas the bonding mode is excited with a probability density that strongly depends on $\bar{d}$, which goes from $\bar{P}_{pl}^{-} < \bar{P}_{pl}^{+}$ for $\bar{d} = 0.1$ to $\bar{P}_{pl}^{-} > \bar{P}_{pl}^{+}$ for $\bar{d} = 1$. This may be related to the strong sensitivity of the bonding mode eigenfrequency $\bar{\omega}_{-}(\bar{k})$ on variations in the interlayer distance. On the other hand, we recall the relation $\bar{P}_{ohm,2}(\bar{\omega}) < \bar{P}_{ohm,1}(\bar{\omega})$ between the integrated ohmic energy losses in the lower and upper graphene layers, seen in Figure 5 at frequencies $\bar{\omega} \lesssim 1$ for both $\bar{d} = 1$ and 0.1, which primarily results from the interference terms with $\sin(\omega d/v)$ in eq 11. Therefore, it appears that the interlayer distance plays different and somewhat intricate roles in the modal decomposition of plasmon excitation probability and the layer-wise decompositions of ohmic losses at sub-THz frequencies.

Different Conductivities. In the previous subsection, we have analyzed asymmetries, which arise in the ohmic energy losses and radiation spectra with respect to the direction of the external particle trajectory, for a symmetric structure consisting of two graphene layers with equal conductivities. In this subsection we focus on a structure that is inherently asymmetric due to different doping densities of two graphene layers, $|n_1| \neq |n_2|$, which we parametrize by the ratio $\rho = k_{F,1}/k_{F,2} = \sqrt{|n_1|/|n_2|}$. Some of the results shown in this subsection will exhibit an asymmetry with respect to changing the ratio from a value $\rho > 1$ to $1/\rho$, which is equivalent to changing the direction of motion of the external charged particle, while other results will not exhibit such asymmetry. Accordingly, whenever a set of results for some $\rho > 1$ cannot be distinguished from results for the corresponding value $1/\rho$, we shall only discuss a range of values $\rho \geq 1$. Otherwise, we shall show results for both $\rho > 1$ and the corresponding $1/\rho$ values.

In the SI, we discuss the effects of variation in the asymmetry ratio ρ on the dispersion relations for the hybridized DPP

DOI: 10.1021/acsphotonics.7b00344
ACS Photonics XXXX, XXX, XXX−XXX

modes with eigenfrequencies $\bar{\omega}_{\mp}(\bar{k})$. We find that the distance between $\bar{\omega}_{-}(\bar{k})$ and $\bar{\omega}_{+}(\bar{k})$ increases as the ratio ρ departs further away from the value $\rho = 1$ and that the mode with lower frequency $\bar{\omega}_{-}(\bar{k})$ is much more affected by variations in ρ than the mode with higher frequency $\bar{\omega}_{+}(\bar{k})$. In particular, in the limit of long wavelengths, $kd = \bar{k}\bar{d} \ll 1$, we find for the higher-frequency mode $\bar{\omega}_{+} \approx 2\sqrt{-2 + \sqrt{4 + \bar{k}^2}}$, which is independent of the ratio ρ and corresponds to a single graphene layer with the effective Fermi wavenumber $k_F = k_{F,1} + k_{F,2}$, whereas the lower-frequency mode exhibits quasi-acoustic dispersion $\bar{\omega}_{-} \approx \sqrt{\frac{8\rho\bar{d}}{(1+\rho)^2 + 8\rho\bar{d}}}\,\bar{k}$, which in the limit of short distances, $\bar{d} \ll 1$, becomes independent of retardation effects.

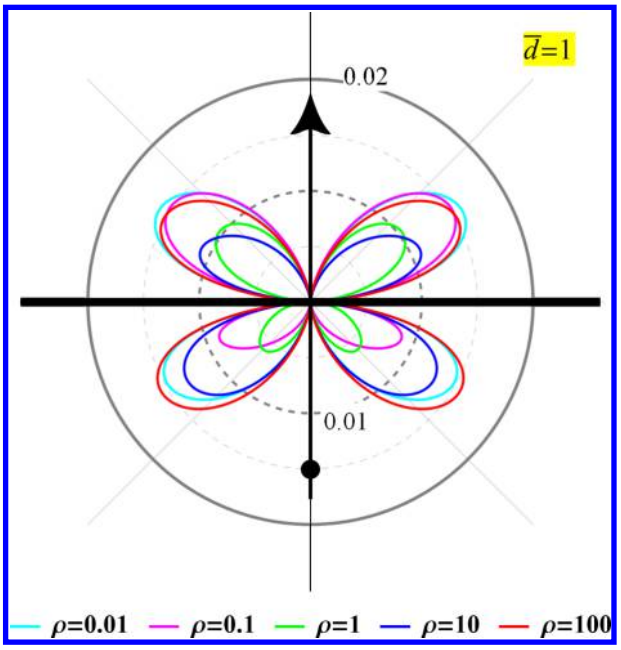

Figure 7. Angular distribution of the joint spectral density of radiation losses, $\bar{S}(\theta,\bar{\omega})$, at fixed frequency $\bar{\omega} = 1$, for two graphene layers at a distance $\bar{d} = 1$, having equal damping rates, $\bar{\gamma}_1 = \bar{\gamma}_2 = 0.1$, but different doping densities giving rise to several values of the asymmetry ratio ρ. The reduced speed of the external electron is $\beta = 0.5$.

Figure 7 displays angular distribution of the joint spectral density of radiation losses, $\bar{S}(\theta, \bar{\omega})$, which we show in reduced units using the normalization factor $\mathcal{S}_c = e^2/c$ for $\bar{d} = 1$ at fixed frequency $\bar{\omega} = 1$, for several values of the asymmetry ratio in the range $0.01 \le \rho \le 100$. Notice that the curve with $\rho = 1$ is reproduced from Figure 3b for $\bar{\omega} = 1$ in order to recall that there exists an asymmetry between the radiation patterns emitted in the upper and lower half-spaces. While that figure showed substantial variability of the patterns for different $\bar{\omega}$ values due to the oscillating terms in eq 12, we see in Figure 7 that, for fixed $\bar{\omega} = 1$ and fixed $\bar{d} = 1$, there also exists great variability with ρ in the asymmetry of the emitted radiation patterns, especially in the interval $0.1 \le \rho \le 10$.

Furthermore, it should be noted in Figure 7 that the emitted spectra in the upper and lower half-spaces are not completely reversed when going from $\rho = 0.1$ to $\rho = 10$, which points to an interesting interplay of the inherent asymmetry of a structure with $\rho \neq 1$ and the asymmetry due to retardation effects upon changing the direction of motion of the charged particle. On the other hand, it seems that the asymmetry between the spectra emitted in the upper and lower half-spaces is significantly reduced when either $\rho = 0.01$ or $\rho = 100$, corresponding to situations when one graphene layer is almost removed from the structure on the account of having a negligibly small charge carrier density compared to the other layer. Finally, it is worthwhile to remark that, similarly to the trends discussed in Figure 3a, the asymmetry with respect to varying the ratio ρ is also diminished when $\bar{\omega}\bar{d} \ll 1$. This describes a situation where the two graphene layers are almost blended into a single layer with an effective Fermi wavenumber $k_F = k_{F,1} + k_{F,2}$.[55]

Figure 8 displays the integrated probability densities for the total energy losses of the external electron, $\bar{P}_{ext}(\bar{\omega})$(solid lines),

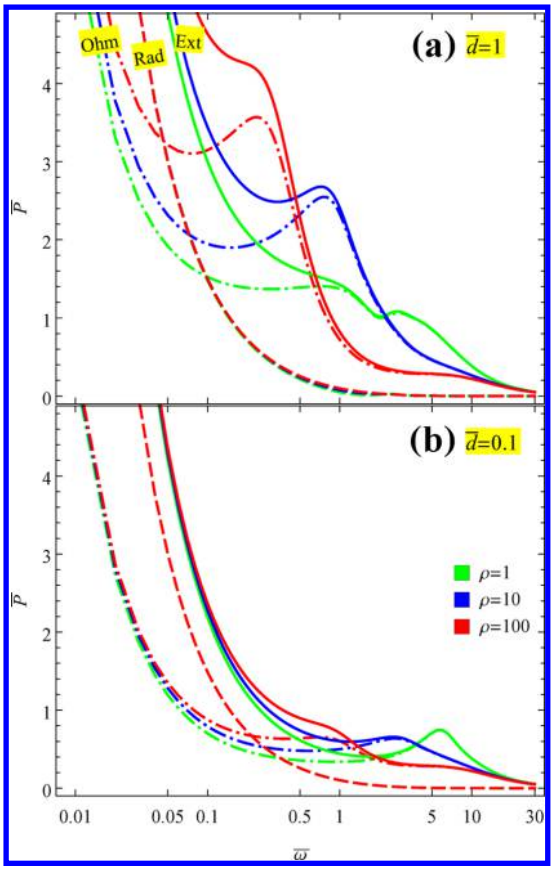

Figure 8. Integrated probability densities for the total energy losses of the external electron, $\bar{P}_{ext}(\bar{\omega})$ (solid lines), total ohmic losses, $\bar{P}_{ohm}(\bar{\omega})$ (dot-dashed lines), and the total radiation losses, $\bar{P}_{rad}(\bar{\omega})$ (dashed lines), are shown in reduced units for two graphene layers with equal damping rates, $\bar{\gamma}_1 = \bar{\gamma}_2 = 0.1$, at distances (a) $\bar{d} = 1$ and (b) $\bar{d} = 0.1$, for three values of the asymmetry ratio, $\rho = 1$, 10, and 100. The reduced speed of the external electron is $\beta = 0.5$.

total ohmic losses, $\bar{P}_{ohm}(\bar{\omega})$ (dash-dotted lines), and the total radiation losses, $\bar{P}_{rad}(\bar{\omega})$ (dashed lines), which we show in reduced units using the normalization factor $P_c = \frac{4}{\pi}\frac{v_B}{c}\frac{1}{\hbar\omega_c}$ for (a) $\bar{d} = 1$ and (b) $\bar{d} = 0.1$, and for three values of the asymmetry ratio, $\rho = 1$, 10, and 100. Note that each set of curves upholds the conservation of energy in the sense $\bar{P}_{ext}(\bar{\omega}) = \bar{P}_{ohm}(\bar{\omega}) + \bar{P}_{rad}(\bar{\omega})$. One notices in the panel (a) of Figure 8 a progression of peak structures in $\bar{P}_{ext}(\bar{\omega})$, which grow in magnitude and move to lower frequencies with increasing ρ values. When $\rho = 1$

DOI: 10.1021/acsphotonics.7b00344
ACS Photonics XXXX, XXX, XXX−XXX

and 10, those structures are related to ohmic losses, $\overline{P}_{ohm}(\overline{\omega})$, which dominate at frequencies $\overline{\omega} \gtrsim 1$, whereas radiation losses, $\overline{P}_{rad}(\overline{\omega})$, are comparable to the ohmic losses when $\overline{\omega} \sim 0.1$ and become dominant for $\overline{\omega} \lesssim 0.1$. On the other hand, when $\rho = 100$ in Figure 8a, a peak in $\overline{P}_{ohm}(\overline{\omega})$ that occurs at a frequency $0.1 < \overline{\omega} < 0.5$, is converted to a shoulder in $\overline{P}_{ext}(\overline{\omega})$ in the same frequency interval owing to the presence of a strongly increasing $\overline{P}_{rad}(\overline{\omega})$ at decreasing frequencies. In the case of a shorter interlayer distance $\overline{d} = 0.1$ in Figure 8b, the peak structures that arise from $\overline{P}_{ohm}(\overline{\omega})$ are moved to higher frequencies, so that the effects of radiation losses are not so prominent in the features observed in $\overline{P}_{ext}(\overline{\omega})$. It is interesting to observe in Figure 8a that the total energy losses of the external electron, as well as the ohmic losses, decrease in magnitude with increasing ρ at frequencies $\overline{\omega} \gtrsim 2$, whereas the opposite is true for those losses at frequencies $\overline{\omega} \lesssim 0.5$. Similar observations are made in Figure 8b, but for frequencies $\overline{\omega} \gtrsim 5$ and $\overline{\omega} \lesssim 1$, respectively.

Finally, it is noteworthy in Figure 8 that the integrated radiation energy losses, $\overline{P}_{rad}(\overline{\omega})$, do not show any appreciable dependence on the value of the asymmetry ratio ρ or on the interlayer distance $\overline{d}$. This is similar to observations made in Figure 4a regarding the $\overline{d}$-dependence of $\overline{P}_{rad}(\overline{\omega})$. Our calculations for directional decomposition of the radiation losses (not shown) also confirm that the integrated probability densities for radiation losses in the upper and lower half-spaces, $\overline{P}^{\uparrow}_{rad}(\overline{\omega})$ and $\overline{P}^{\downarrow}_{rad}(\overline{\omega})$, do not show any appreciable dependence on ρ or $\overline{d}$, similar to the observations made in Figure 5a.

In the SI we further analyze effects of the asymmetry ratio ρ in the layer-wise decomposition of the integrated probability density for ohmic energy losses, $\overline{P}_{ohm}(\overline{\omega}) = \overline{P}_{ohm,1}(\overline{\omega}) + \overline{P}_{ohm,2}(\overline{\omega})$, and find much larger differences between contributions from the lower and upper graphene layers for values $\rho \neq 1$ when $\overline{d} = 1$ than differences observed in Figure 5a for $\rho = 1$. This is further elucidated in the SI by analyzing modal decomposition of the probability density for plasmon excitations, $\overline{P}_{pl}(\overline{\omega}) = \overline{P}^{-}_{pl}(\overline{\omega}) + \overline{P}^{+}_{pl}(\overline{\omega})$, which reveals an intricate interplay between the effects of increasing interlayer distance $\overline{d}$ and variations in the asymmetry ratio ρ in ohmic losses at frequencies $\overline{\omega} \gtrsim 1$.

CONCLUSIONS

We have presented a fully relativistic treatment of energy losses and transition radiation from multilayer graphene traversed by an electron at a speed typical for Transmission Electron Microscope. Adopting the Drude model for the conductivity of graphene we have concentrated on a THz range of frequencies and analyzed the case of two graphene layers. Our main interest was to reveal the effects of interlayer distance d and the difference in doping densities of charge carriers in those layers, n_1 and n_2, as the two parameters that are most relevant for the design of graphene-based nanophotonic and nanoplasmonic devices. For this structure, strong hybridization takes place between the Dirac plasmon polaritons in individual graphene layers, giving rise to a low-frequency, quasi-acoustic mode designated as bonding mode, and a high-frequency, quasi-optical mode designated as antibonding mode.

Our model uses standard definitions, which demonstrate that probability density of the total energy loss of an external charged particle is given by a sum of the probability densities for ohmic losses in graphene layers and the energy emitted in the far-field region as transition radiation. In particular, ohmic losses are dominated by excitations of the bonding and antibonding modes at frequencies located outside the light cone, and are accompanied by release of the Joule heat in the presence of finite damping rates in graphene, taking place at frequencies located both outside and inside the light cone.

We have seen that the effects of retardation are quantitatively relevant for frequencies $\lesssim$10 THz for typical doping densities of graphene. Moreover, the total energy loss of the external particle is completely determined by the ohmic losses for frequencies $\gtrsim$1 THz, whereas radiation losses are comparable to the ohmic losses around ∼1 THz, and they become dominant in a sub-THz range of frequencies.

Our calculations also aimed at analyzing interferences due to retardation effects, which may give rise to observable asymmetries in directional decomposition of the radiation emitted in the upper and lower half-spaces, layer-wise decomposition of the ohmic losses in graphene, and modal decomposition of the excitation probability density for hybridized plasmon polariton modes.

We have found that differences between the angular distributions of radiation spectra emitted in the upper and lower half-spaces show strong asymmetry with respect to the direction of motion of the external charged particle for frequencies satisfying $\omega \gtrsim c/d$, where c is the speed of light in vacuum. This effect of retardation was observed when the graphene layers have equal doping densities, and was found to be greatly magnified when there is a difference in doping densities, such that the ratio of the Fermi wavenumbers in graphene layers, $\rho = k_{F,1}/k_{F,2} = \sqrt{|n_1|/|n_2|}$, falls in an interval $0.1 \lesssim \rho \lesssim 10$. This asymmetry in the radiation spectra is reduced when $\omega \lesssim c/d$ or when the ratio ρ falls outside the indicated interval. On the other hand, when the radiated spectra are integrated over all angles, both their asymmetry and their dependence on the interlayer distance and the ratio ρ are diminished.

We have further discovered a surprising asymmetry in ohmic energy losses at frequencies $\omega \lesssim k_F v_F v_B/c$ (i.e., sub-THz frequencies for typical doping densities), such that a graphene layer with given doping density absorbs more ohmic energy when it is first traversed by the external charged particle than when it is last traversed. While this is true for both the case of graphene layers with equal doping densities and the case of layers with different doping densities for a distance $d \sim c^2/(v_B v_F k_F)$ (≈ 73 μm for typical doping densities), a reduction of the interlayer distance diminishes such asymmetry in ohmic losses.

At higher frequencies (typically supra-THz), excitations of the hybridized Dirac plasmon polariton modes play a decisive role in the ohmic energy losses and, accordingly, in the total energy losses of the external charged particle. We have found that, if two graphene layers have equal doping densities, then there is onset of strong oscillations in the modal decomposition at a frequency $\omega \sim \pi v/d$ (where v is the speed of the external particle), giving rise to observable interference features in the ohmic energy spectra. If the graphene layers have sufficiently different doping densities, then oscillations subside in the modal decomposition. In that case it was found that the graphene layer with smaller doping density predominantly absorbs ohmic energy by excitation of the bonding mode, whereas the layer with higher doping density absorbs ohmic energy by excitation of the antibonding mode. In general, ohmic losses at supra-THz frequencies were found to be strongly dependent on both d and ρ in a nontrivial manner,

DOI: 10.1021/acsphotonics.7b00344
ACS Photonics XXXX, XXX, XXX−XXX

mostly owing to the sensitivity of the bonding mode to variations in values of those two parameters.

Besides the effects of varying interlayer distance and doping densities of graphene layers, we have also investigated in the Supporting Information (SI) the effects of varying damping rates in graphene layers and varying speed of the external electron. As in the case of single-layer graphene,[55] we have found a strong increase in ohmic losses at sub-THz frequencies with increasing damping rate(s). In particular, when graphene layers are characterized with different damping rates, $\gamma_1 \neq \gamma_2$, there arises a surprisingly large asymmetry in the layer-wise decomposition of ohmic losses with respect to the direction of motion of the external charged particle, even in the case of graphene layers with nominally equal doping densities. On the other hand, radiative losses were found in the SI to be rather independent of the damping rate when $\gamma \lesssim 0.1$ THz, but strongly decreasing when the damping rate increases above $\gamma \sim 1$ THz, while still exhibiting directional asymmetry in the angular spectra at frequencies $\omega \gtrsim c/d$.

As for the speed v of the external electron, we have found a strong increase in the magnitude of radiation losses with increasing v, as expected. While the overall shapes of the angular spectra of emitted radiation change with increasing v in a manner similar to that observed for single-layer graphene,[55] the directional asymmetry in the spectra from two layers is observed over a broad range of the electron speeds for large interlayer distances. On the other hand, ohmic losses also exhibit a strong increase in magnitude with increasing v at frequencies $\omega \lesssim 1$ THz, whereas this effect is reversed at frequencies $\omega \gtrsim 1$ THz. Finally, an analysis of the average numbers of the hybridized DPP modes, performed in the SI, has revealed an intricate interplay between the speed v and the intergraphene distance.

■ ASSOCIATED CONTENT

Supporting Information

The Supporting Information is available free of charge on the ACS Publications website at DOI: 10.1021/acsphotonics.7b00344.

Elaboration on the self-consistent theory of induced electromagnetic fields and definitions of probability densities for a general N-layer problem; detailed formulation of the two-layer graphene problem with modal decomposition of plasmon excitations; additional results, including the effects of damping rates and external particle's speed (PDF).

■ AUTHOR INFORMATION

Corresponding Authors

*E-mail: kakbari@uwaterloo.ca.
*E-mail: zmiskovi@uwaterloo.ca.
*E-mail: segui@cab.cnea.gov.ar.

ORCID

Zoran L. Mišković: 0000-0003-3882-8930

Notes

The authors declare no competing financial interest.

■ ACKNOWLEDGMENTS

Argentinean team acknowledges the financial support from CONICET (PIP 11220120100374) and ANPCyT (PICT 2012-1136) from Argentina. Z.L.M. acknowledges support from the Natural Sciences and Engineering Research Council of Canada (Grant No. 2016-03689).

■ REFERENCES

(1) Bonaccorso, F.; Sun, Z.; Hasan, T.; Ferrari, A. C. Graphene photonics and optoelectronics. *Nat. Photonics* **2010**, *4*, 611−622.
(2) Grigorenko, A. N.; Polini, M.; Novoselov, K. S. Graphene plasmonics. *Nat. Photonics* **2012**, *6*, 749−758.
(3) Garcia de Abajo, F. J. Graphene Plasmonics: Challenges and Opportunities. *ACS Photonics* **2014**, *1*, 135−152.
(4) Aliofkhazraei, M.; Ali, N.; Milne, W.; Ozkan, C.; Mitura, S.; Gervasoni, J. *Graphene Science Handbook, Six-Vol. Set*; Taylor & Francis, 2016.
(5) Woessner, A.; Lundeberg, M. B.; Gao, Y.; Principi, A.; Alonso-González, P.; Carrega, M.; Watanabe, K.; Taniguchi, T.; Vignale, G.; Polini, M.; Hone, J.; Hillenbrand, R.; Koppens, F. H. L. Highly confined low-loss plasmons in graphene-boron nitride heterostructures. *Nat. Mater.* **2014**, *14*, 421−425.
(6) Chen, J.; Badioli, M.; Alonso-Gonzalez, P.; Thongrattanasiri, S.; Huth, F.; Osmond, J.; Spasenovic, M.; Centeno, A.; Pesquera, A.; Godignon, P.; Zurutuza Elorza, A.; Camara, N.; de Abajo, F. J. G.; Hillenbrand, R.; Koppens, F. H. L. Optical nano-imaging of gate-tunable graphene plasmons. *Nature* **2012**, *487*, 77−81.
(7) Fei, Z.; Rodin, A. S.; Andreev, G. O.; Bao, W.; McLeod, A. S.; Wagner, M.; Zhang, L. M.; Zhao, Z.; Thiemens, M.; Dominguez, G.; Fogler, M. M.; Neto, A. H. C.; Lau, C. N.; Keilmann, F.; Basov, D. N. Gate-tuning of graphene plasmons revealed by infrared nano-imaging. *Nature* **2012**, *487*, 82−85.
(8) Castro Neto, A. H.; Guinea, F.; Peres, N. M. R.; Novoselov, K. S.; Geim, A. K. The electronic properties of graphene. *Rev. Mod. Phys.* **2009**, *81*, 109−162.
(9) Bao, Q.; Loh, K. P. Graphene Photonics, Plasmonics, and Broadband Optoelectronic Devices. *ACS Nano* **2012**, *6*, 3677−3694.
(10) Polat, E. O.; Uzlu, H. B.; Balci, O.; Kakenov, N.; Kovalska, E.; Kocabas, C. Graphene-Enabled Optoelectronics on Paper. *ACS Photonics* **2016**, *3*, 964−971.
(11) Echtermeyer, T. J.; Britnell, L.; Jasnos, P. K.; Lombardo, A.; Gorbachev, R. V.; Grigorenko, A. N.; Geim, A. K.; Ferrari, A. C.; Novoselov, K. S. Strong plasmonic enhancement of photovoltage in graphene. *Nat. Commun.* **2011**, *2*, 458.
(12) Miao, X.; Tongay, S.; Petterson, M. K.; Berke, K.; Rinzler, A. G.; Appleton, B. R.; Hebard, A. F. High Efficiency Graphene Solar Cells by Chemical Doping. *Nano Lett.* **2012**, *12*, 2745−2750.
(13) Wu, L.; Chu, H. S.; Koh, W. S.; Li, E. P. Highly sensitive graphene biosensors based on surface plasmon resonance. *Opt. Express* **2010**, *18*, 14395−14400.
(14) Wu, L.; Guo, J.; Xu, H.; Dai, X.; Xiang, Y. Ultrasensitive biosensors based on long-range surface plasmon polariton and dielectric waveguide modes. *Photonics Res.* **2016**, *4*, 262−266.
(15) Salihoglu, O.; Balci, S.; Kocabas, C. Plasmon-polaritons on graphene-metal surface and their use in biosensors. *Appl. Phys. Lett.* **2012**, *100*, 213110.
(16) Morales-Narvaez, E.; Baptista-Pires, L.; Zamora-Galvez, A.; Merkoci, A. Graphene-Based Biosensors: Going Simple. *Adv. Mater.* **2017**, *29*, 1604905.
(17) Zhu, M.; Chen, P.; Liu, M. Graphene Oxide Enwrapped Ag/AgX (X = Br, Cl) Nanocomposite as a Highly Efficient Visible-Light Plasmonic Photocatalyst. *ACS Nano* **2011**, *5*, 4529−4536.
(18) Chuang, M.-K.; Lin, S.-W.; Chen, F.-C.; Chu, C.-W.; Hsu, C.-S. Gold nanoparticle-decorated graphene oxides for plasmonic-enhanced polymer photovoltaic devices. *Nanoscale* **2014**, *6*, 1573−1579.
(19) Low, T.; Avouris, P. Graphene Plasmonics for Terahertz to Mid-Infrared Applications. *ACS Nano* **2014**, *8*, 1086−1101.
(20) Bitounis, D.; Ali-Boucetta, H.; Hong, B. H.; Min, D.-H.; Kostarelos, K. Prospects and Challenges of Graphene in Biomedical Applications. *Adv. Mater.* **2013**, *25*, 2258−2268.
(21) Ma, H.; Jiang, C.; Zhai, D.; Luo, Y.; Chen, Y.; Lv, F.; Yi, Z.; Deng, Y.; Wang, J.; Chang, J.; Wu, C. A Bifunctional Biomaterial with

DOI: 10.1021/acsphotonics.7b00344
ACS Photonics XXXX, XXX, XXX−XXX

Photothermal Effect for Tumor Therapy and Bone Regeneration. *Adv. Funct. Mater.* **2016**, *26*, 1197−1208.
(22) Butler, S. Z.; et al. Progress, Challenges, and Opportunities in Two-Dimensional Materials Beyond Graphene. *ACS Nano* **2013**, *7*, 2898−2926.
(23) Choi, K.; Lee, Y. T.; Im, S. Two-dimensional van der Waals nanosheet devices for future electronics and photonics. *Nano Today* **2016**, *11*, 626−643.
(24) Mak, K. F.; Shan, J. Photonics and optoelectronics of 2D semiconductor transition metal dichalcogenides. *Nat. Photonics* **2016**, *10*, 216−226.
(25) Eberlein, T.; Bangert, U.; Nair, R. R.; Jones, R.; Gass, M.; Bleloch, A. L.; Novoselov, K. S.; Geim, A.; Briddon, P. R. Plasmon spectroscopy of free-standing graphene films. *Phys. Rev. B: Condens. Matter Mater. Phys.* **2008**, *77*, 233406.
(26) Wachsmuth, P.; Hambach, R.; Kinyanjui, M. K.; Guzzo, M.; Benner, G.; Kaiser, U. High-energy collective electronic excitations in free-standing single-layer graphene. *Phys. Rev. B: Condens. Matter Mater. Phys.* **2013**, *88*, 075433.
(27) Nelson, F. J.; Idrobo, J.-C.; Fite, J. D.; Miskovic, Z. L.; Pennycook, S. J.; Pantelides, S. T.; Lee, J. U.; Diebold, A. C. Electronic Excitations in Graphene in the 1−50 eV Range: The π and $\pi + \sigma$ Peaks Are Not Plasmons. *Nano Lett.* **2014**, *14*, 3827−3831.
(28) Kapetanakis, M. D.; Zhou, W.; Oxley, M. P.; Lee, J.; Prange, M. P.; Pennycook, S. J.; Idrobo, J. C.; Pantelides, S. T. Low-loss electron energy loss spectroscopy: An atomic-resolution complement to optical spectroscopies and application to graphene. *Phys. Rev. B: Condens. Matter Mater. Phys.* **2015**, *92*, 125147.
(29) Wang, Z.; Li, T.; Almdal, K.; Asger Mortensen, N.; Xiao, S.; Ndoni, S. Experimental demonstration of graphene plasmons working close to the near-infrared window. *Opt. Lett.* **2016**, *41*, 5345−5348.
(30) Wallace, P. R. The Band Theory of Graphite. *Phys. Rev.* **1947**, *71*, 622−634.
(31) Das Sarma, S.; Adam, S.; Hwang, E. H.; Rossi, E. Electronic transport in two-dimensional graphene. *Rev. Mod. Phys.* **2011**, *83*, 407−470.
(32) Xiao, S.; Zhu, X.; Li, B.-H.; Mortensen, N. A. Graphene-plasmon polaritons: From fundamental properties to potential applications. *Front. Phys.* **2016**, *11*, 117801.
(33) Deng, B.; Guo, Q.; Li, C.; Wang, H.; Ling, X.; Farmer, D. B.; Han, S.-j.; Kong, J.; Xia, F. Coupling-Enhanced Broadband Mid-infrared Light Absorption in Graphene Plasmonic Nanostructures. *ACS Nano* **2016**, *10*, 11172−11178.
(34) Jablan, M.; Buljan, H.; Soljačić, M. Transverse electric plasmons in bilayer graphene. *Opt. Express* **2011**, *19*, 11236−11241.
(35) Gumbs, G.; Iurov, A.; Wu, J.-Y.; Lin, M. F.; Fekete, P. Plasmon Excitations of Multi-layer Graphene on a Conducting Substrate. *Sci. Rep.* **2016**, *6*, 21063.
(36) Crassee, I.; Orlita, M.; Potemski, M.; Walter, A. L.; Ostler, M.; Seyller, T.; Gaponenko, I.; Chen, J.; Kuzmenko, A. B. Intrinsic Terahertz Plasmons and Magnetoplasmons in Large Scale Monolayer Graphene. *Nano Lett.* **2012**, *12*, 2470−2474.
(37) Gómez-Santos, G.; Stauber, T. Plasmons in layered structures including graphene. *New J. Phys.* **2012**, *14*, 105018.
(38) Gonçalves, P. A. D.; Dias, E. J. C.; Xiao, S.; Vasilevskiy, M. I.; Mortensen, N. A.; Peres, N. M. R. Graphene Plasmons in Triangular Wedges and Grooves. *ACS Photonics* **2016**, *3*, 2176−2183.
(39) Hwang, E. H.; Das Sarma, S. Plasmon modes of spatially separated double-layer graphene. *Phys. Rev. B: Condens. Matter Mater. Phys.* **2009**, *80*, 205405.
(40) Yan, H.; Li, X.; Chandra, B.; Tulevski, G.; Wu, Y.; Freitag, M.; Zhu, W.; Avouris, P.; Xia, F. Tunable infrared plasmonic devices using graphene/insulator stacks. *Nat. Nanotechnol.* **2012**, *7*, 330−334.
(41) Stauber, T. Plasmonics in Dirac systems: from graphene to topological insulators. *J. Phys.: Condens. Matter* **2014**, *26*, 123201.
(42) Ritchie, R. H. Plasma Losses by Fast Electrons in Thin Films. *Phys. Rev.* **1957**, *106*, 874−881.
(43) Powell, C. J.; Swan, J. B. Origin of the Characteristic Electron Energy Losses in Aluminum. *Phys. Rev.* **1959**, *115*, 869−875.
(44) Rossouw, D.; Couillard, M.; Vickery, J.; Kumacheva, E.; Botton, G. A. Multipolar Plasmonic Resonances in Silver Nanowire Antennas Imaged with a Subnanometer Electron Probe. *Nano Lett.* **2011**, *11*, 1499−1504.
(45) Kociak, M.; Stephan, O. Mapping plasmons at the nanometer scale in an electron microscope. *Chem. Soc. Rev.* **2014**, *43*, 3865−3883.
(46) García de Abajo, F. J. Optical excitations in electron microscopy. *Rev. Mod. Phys.* **2010**, *82*, 209−275.
(47) Coenen, T.; Brenny, B. J.; Vesseur, E. J.; Polman, A. Cathodoluminescence microscopy: Optical imaging and spectroscopy with deep-subwavelength resolution. *MRS Bull.* **2015**, *40*, 359−365.
(48) Ochiai, T. Efficiency and Angular Distribution of Graphene-Plasmon Excitation by Electron Beam. *J. Phys. Soc. Jpn.* **2014**, *83*, 54705.
(49) Mendis, B. G.; Howkins, A.; Stowe, D.; Major, J. D.; Durose, K. The role of transition radiation in cathodoluminescence imaging and spectroscopy of thin-foils. *Ultramicroscopy* **2016**, *167*, 31−42.
(50) Stöger-Pollach, M.; Kachtík, L.; Miesenberger, B.; Retzl, P. Transition radiation in EELS and cathodoluminescence. *Ultramicroscopy* **2017**, *173*, 31−35.
(51) Zhan, T.; Han, D.; Hu, X.; Liu, X.; Chui, S.-T.; Zi, J. Tunable terahertz radiation from graphene induced by moving electrons. *Phys. Rev. B: Condens. Matter Mater. Phys.* **2014**, *89*, 245434.
(52) Zhao, T.; Gong, S.; Hu, M.; Zhong, R.; Liu, D.; Chen, X.; Zhang, P.; Wang, X.; Zhang, C.; Wu, P.; Liu, S. Coherent and Tunable Terahertz Radiation from Graphene Surface Plasmon Polarirons Excited by Cyclotron Electron Beam. *Sci. Rep.* **2015**, *5*, 16059.
(53) Wong, L. J.; Kaminer, I.; Ilic, O.; Joannopoulos, J. D.; Soljačić, M. Towards graphene plasmon-based free-electron infrared to X-ray sources. *Nat. Photonics* **2015**, *10*, 46−52.
(54) Liu, S.; Hu, M.; Zhong, R.; Chen, X.; Zhang, P.; Gong, S.; Zhao, T. Electron beam excitation of surface plasmon polaritons and transformation into electromagnetic radiation. *Terahertz Sci. Technol.* **2015**, *8*, 69−84.
(55) Miskovic, Z. L.; Segui, S.; Gervasoni, J. L.; Arista, N. R. Energy losses and transition radiation produced by the interaction of charged particles with a graphene sheet. *Phys. Rev. B: Condens. Matter Mater. Phys.* **2016**, *94*, 125414.
(56) Guinea, B. W.; Stauber, T.; Sols, F. Dynamical polarization of graphene at finite doping. *New J. Phys.* **2006**, *8*, 318.
(57) Hwang, E. H.; Das Sarma, S. Dielectric function, screening, and plasmons in two-dimensional graphene. *Phys. Rev. B: Condens. Matter Mater. Phys.* **2007**, *75*, 205418.
(58) Jackson, J. D. *Classical Electrodynamics*, 3rd ed.; Wiley: New York, 1999.
(59) Stratton, J. A. *Electromagnetic Theory*; McGraw-Hill: New York, 1941.
(60) Novko, D.; Šunjić, M.; Despoja, V. Optical absorption and conductivity in quasi-two-dimensional crystals from first principles: Application to graphene. *Phys. Rev. B: Condens. Matter Mater. Phys.* **2016**, *93*, 125413.
(61) Xia, F.; Wang, H.; Xiao, D.; Dubey, M.; Ramasubramaniam, A. Two-dimensional material nanophotonics. *Nat. Photonics* **2014**, *8*, 899−907.
(62) Nemilentsau, A.; Low, T.; Hanson, G. Anisotropic 2D Materials for Tunable Hyperbolic Plasmonics. *Phys. Rev. Lett.* **2016**, *116*, 066804.

DOI: 10.1021/acsphotonics.7b00344
ACS Photonics XXXX, XXX, XXX−XXX